

Carbon chain diversity in L1544 and IRAS 16293-2422: an astrochemical pathfinder study for the SKAO

Lisa Giani,¹  Eleonora Bianchi,¹ Anthony Remijan,² Claudio Codella,^{1,3} Giovanni Sabatini,¹ Linda Podio,¹ Cecilia Ceccarelli,³ Marta De Simone,⁴ Nadia Balucani,⁵ Paola Caselli,⁶ Eric Herbst,^{7,8} Francois Lique,⁹ Silvia Spezzano,⁶ Charlotte Vastel¹⁰ and Brett McGuire^{11,12}

¹INAF, Osservatorio Astrofisico di Arcetri, Largo E. Fermi 5, I-50125, Firenze, Italy

²National Radio Astronomy Observatory, Charlottesville, VA 22903, USA

³Univ. Grenoble Alpes, CNRS, IPAG, 38000 Grenoble, France

⁴European Southern Observatory, Karl-Schwarzschild Str. 2, 85748 Garching bei München, Germany

⁵Dipartimento di Chimica, Biologia e Biotecnologie, Via Elce di Sotto 8, 06123 Perugia, Italy

⁶Max-Planck-Institut für extraterrestrische Physik (MPE), Giessenbachstrasse 1, 85748 Garching, Germany

⁷Department of Chemistry, University of Virginia, Charlottesville, VA 22904, USA

⁸Department of Astronomy, University of Virginia, Charlottesville, VA 22904, USA

⁹Université du Rennes, CNRS, IPR (Institut de Physique de Rennes)UMR 6251, F-35000 Rennes, France

¹⁰IRAP, Université de Toulouse, CNRS, UPS, CNES, 31400 Toulouse, France

¹¹Department of Chemistry, Massachusetts Institute of Technology, Cambridge, MA 02139, USA

¹²National Radio Astronomy Observatory, Charlottesville, VA 22903, USA

Accepted XXX. Received YYY; in original form ZZZ

ABSTRACT

Astrochemical observations have revealed a surprisingly high level of chemical complexity, including long carbon chains, in the earliest stages of Sun-like star formation. The origin of these species and whether they undergo further growth, possibly contributing to the molecular complexity of planetary systems, remain open questions. We present recent observations performed using the 100-m Green Bank Telescope of the prestellar core L1544, and the protostellar system IRAS 16293–2422. In L1544, we detected several complex carbon-bearing species, including C₂S, C₃S, C₃N, c-C₃H, C₄H and C₆H, complementing previously reported emission of cyanopolyyynes. In IRAS 16293–2422, we detected c-C₃H and, for the first time, HC₇N. Thanks to the high spectral resolution, we refine the rest frequencies of several c-C₃H and C₆H transitions. We perform radiative transfer analysis, highlighting a chemical difference between the two sources: IRAS 16293–2422 shows column densities 10 to 100 times lower than L1544. We perform astrochemical modeling, employing an up-to-date chemical network with revised reaction rates. Models reproduce the general trends, with cyanopolyyne and polyyynyl radical abundances decreasing as molecular size increases, but underestimate the abundances of cyanopolyyynes longer than HC₅N by up to two orders of magnitude. Current models, which include the dominant neutral–neutral formation routes, cannot account for this discrepancy, suggesting that the chemical network is incomplete. We propose that additional ion–molecule reactions are crucial for the formation of these species. Developing a more comprehensive chemical network for long carbon chains is essential for accurately interpreting present and future observations.

Key words: Astrochemistry — Stars: formation — Interstellar medium — ISM: molecules — ISM: abundances

1 INTRODUCTION

The formation of a Solar-type star and its planetary system begins with a prestellar core, a dense ($\geq 10^5$ cm⁻³) and cold (~ 10 K) condensation of gas typically spanning $\sim 10^3$ – 10^4 au which eventually collapses under its own gravity (e.g. Benson & Myers 1989; Bergin & Tafalla 2007; Keto & Caselli 2008). As the collapse proceeds, a protostar forms in the central region, heating the gas and generating shocks in the surrounding medium (e.g. Stahler & Palla

2004). A surprisingly rich chemistry has been observed even in the initial stages of this process, marked by the gas-phase detection of complex molecules relevant for the formation of prebiotic species, such as interstellar complex organic molecules (iCOMs, primarily C-bearing species with at least 6 atoms; e.g., Ceccarelli 2004; Herbst & van Dishoeck 2009; Ceccarelli et al. 2023, and references therein). The prestellar phase is particularly rich in deuterated species and iCOMs, which are primarily observed at (sub-)millimeter wavelengths (Crapsi et al. 2005; Caselli & Ceccarelli 2012; Vastel et al. 2014, 2019; Bizzocchi et al. 2014; Jiménez-Serra et al. 2016; Spezzano et al. 2017; Punanova et al. 2018; Scibelli et al. 2024). Fur-

* E-mail: lisa.giani@inaf.it

thermore, recent radio observations of the starless core TMC-1, conducted with the Green Bank Telescope (GBT¹) and the YEBES 40-m², have also revealed an active chemistry of complex carbon-bearing species, including cyclic hydrocarbons such as c-C₉H₈, benzonitrile (c-C₆H₅CN), cyanopyrene (C₁₆H₉CN) and cyanocoronene (C₂₄H₁₁CN) (e.g. McGuire et al. 2020; Cernicharo et al. 2021; Siebert et al. 2022; Sita et al. 2022; Agúndez et al. 2023; Silva et al. 2023; Cernicharo et al. 2023; Fuentetaja et al. 2023; Remijan et al. 2023; Wenzel et al. 2025a,b, and references therein). This peculiar chemistry is still mostly unexplored due to limitations in current radio facilities, but there are hints that it may not be confined to TMC-1 and could be widespread in starless and prestellar cores (Burkhardt et al. 2021). On the other hand, a dichotomy in chemical composition has been revealed in protostellar sources. This is characterized by two extreme cases: hot corinos and Warm Carbon Chain Chemistry (WCCC) sources. Hot corinos are regions approximately 100 au in size, where temperatures reach at least 100 K, causing dust mantles to sublimate and, in turn, increasing the abundance of iCOMs (Cecarelli 2004; Ceccarelli et al. 2023). Conversely, WCCC sources are poor in iCOMs but enriched in unsaturated small carbon chains (such as c-C₃H₂, Sakai et al. 2008; Sakai & Yamamoto 2013; Taniguchi et al. 2024) in regions that can extend up to 1000 au, where temperatures exceed 20 K and CH₄ sublimes. The origin of this chemical diversity remains an open question, and the recent discovery of hybrid sources, such as B335, L483 and IRAS 15398-3359, further complicates the picture (Imai et al. 2016; Oya et al. 2017; Jacobsen et al. 2019; Okuda et al. 2023). While a different duration of the prestellar stage or external UV illumination have been proposed as potential explanations for the varying chemistry, the limited number of observations of complex carbon chains prevents a comprehensive understanding of this dichotomy (Bouvier et al. 2020, 2022). In this work, we present a spectral survey conducted with the GBT in the Ku (13.5 - 15.4 GHz) and X (8.0 - 11.6 GHz) bands, targeting one of the prototypical prestellar cores, L1544, along with the molecular envelope surrounding representative protostars embedded within hot corinos, specifically IRAS 16293-2422. The subsequent sections are organized as follows: Section 2 details the two sources, Section 3 describes the observations, Section 4 presents the results, and Section 5 discusses the origin of the observed chemical diversity. Finally, Section 6 provides the conclusions.

2 THE SAMPLE

We chose as targets two well-studied sources that are prototypical of their evolutionary stage: L1544, a prestellar core, and IRAS 16293-2422, a multiple protostellar system. For both sources, their physical structure is well-known, and they are recognized for hosting a rich chemistry, making them ideal targets for exploring molecular composition at low frequencies.

2.1 The L1544 prestellar core

L1544, located in the Taurus molecular cloud complex at a distance of 170 pc (Galli et al. 2019), is one of the most well-studied prestellar cores. Figure 1 (upper panel) shows L1544 as traced by the *Herschel* continuum map at 350 μ m. Its dense ($\sim 10^6$ cm⁻³) and extremely cold

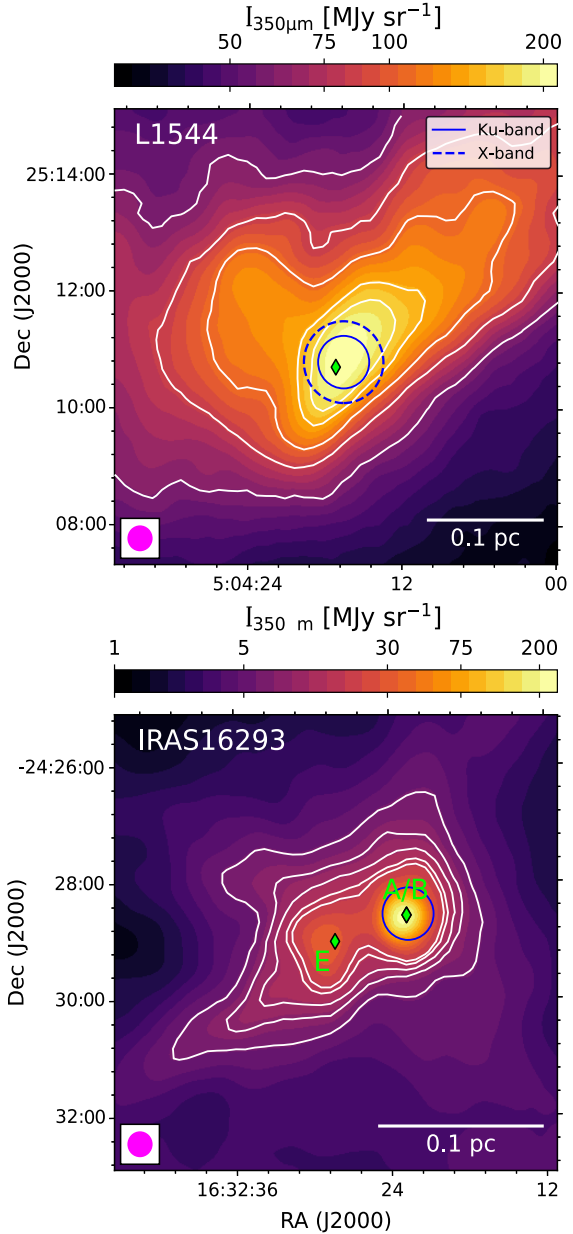


Figure 1. Overview of the L1544 (upper panel) and IRAS 16293-2422 (lower panel) regions as traced by the *Herschel*³ continuum maps at 350 μ m. The white contours correspond to $[5,7,9,12,14]\sigma$, where σ is 12 MJy sr⁻¹ in L1544, and 1.1 MJy sr⁻¹ in IRAS 16293-2422, respectively. The FoVs of the GBT observations are shown as blue circles – solid line for Ku-band and dashed line for X-band observations (see Sect. 3). Green diamonds identify the continuum (~ 1.3 mm) peak position in L1544 (Ward-Thompson et al. 1999) and the position of the A/B, and E objects in IRAS 16293-2422 (Kahle et al. 2023). The size of the *Herschel* beam (25'') is shown in the bottom left corner, while the scale bar is shown in the bottom right.

(down to ~ 7 K) central region (~ 1000 au) exhibits significant CO depletion (Caselli et al. 1999; Crapsi et al. 2007; Caselli et al. 2022). In contrast, the outer regions host various chemical processes that produce iCOMs and carbon chain species, as evidenced by single-dish and interferometric observations (Bizzocchi et al. 2014; Vastel et al. 2014, 2016; Jiménez-Serra et al. 2016; Spezzano et al. 2017; Punanova et al. 2018; Vastel et al. 2018a; Hily-Blant et al. 2018; Vastel et al. 2019; Urso et al. 2019). More specifically, methanol peak is

¹ <https://greenbankobservatory.org/science/telescopes/gbt/>

² <https://rt40m.oan.es/>

³ <https://archives.esac.esa.int/hsa/whsa/>

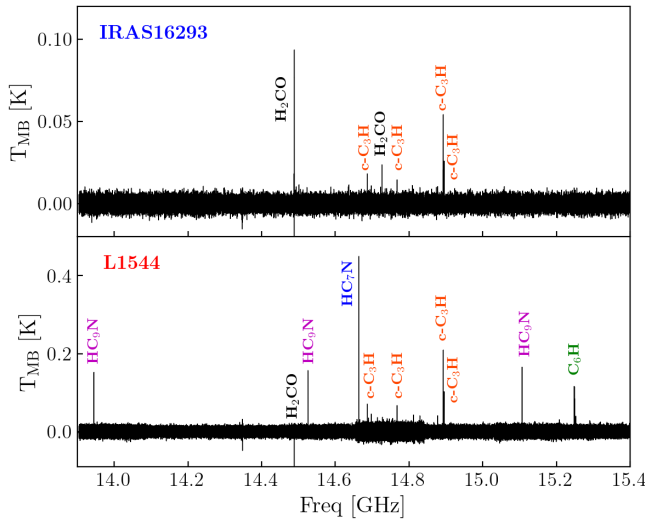


Figure 2. Full continuum-subtracted spectra (in main-beam temperature, T_{MB}) of the IRAS 16293-2422 envelope (Upper panel) and the L1544 prestellar source (Lower panel) observed in Ku Band (13.9 – 15.41 GHz). The brightest lines associated with the detected species (see Tab. 1 for the list of all the detections) are labelled. The L1544 spectrum has a spectral resolution of 1.4 kHz ($\sim 30 \text{ m s}^{-1}$), while the IRAS 16293 spectrum has been here smoothed to 12 kHz ($\sim 240 \text{ m s}^{-1}$) to increase the S/N of the emission lines. In the L1544 spectrum, the H_2CO line at ~ 14.5 GHz is observed in absorption.

about 4000 au north of the core center while emission from $\text{c-C}_3\text{H}_2$ and cyanopolynes peaks in the southern part of the core (Bizzocchi et al. 2014; Spezzano et al. 2016; Lin et al. 2022; Bianchi et al. 2023). This chemical differentiation has been suggested to arise from uneven illumination, influenced by both the asymmetrical 3D structure of the core and its location at the edge of the molecular cloud (Jensen et al. 2023).

2.2 The IRAS 16293–2422 protostellar system

IRAS 16293–2422 (hereafter IRAS 16293) is an archetypical Solar-type star forming region located in the ρ Ophiuchus cloud complex, at a distance $d = 141$ pc (Dzib et al. 2018). IRAS 16293 is the first star forming region where a Class 0 protostar has been identified (Andre et al. 1993), and it has been the target of several studies at both mm- and sub-mm wavelengths that have revealed its physical structure (see the Herschel continuum map at $350 \mu\text{m}$ in Fig. 1 (Lower panel). IRAS 16293 is associated with a large envelope extending up to 6000 au (Castets et al. 2001; Crimier et al. 2010), which surrounds a close binary (protostars A1 and A2) separated by 50 au (Maureira et al. 2020), and a third protostellar object (labelled B) located 600 au (Mundy et al. 1992; Jørgensen et al. 2016) from the A1+A2 system. Within the same molecular cloud lies the prestellar core IRAS 16293 E, located about $90''$ east of the protostellar objects (Loinard et al. 2001). The inner regions of IRAS 16293 A and B are characterized by the presence of hot corinos, where the gas phase abundances of many molecules, particularly iCOMs, increase by several orders of magnitude compared to those in the surrounding envelope. IRAS 16293 has been the preferential target of several unbiased spectral line surveys dedicated to unveiling the chemical composition of star-forming regions, such as CHESS (Ceccarelli et al. 2010), TIMASS (Caux et al. 2011), and PILS (Jørgensen et al. 2016). These stud-

ies have led to the discovery of a large chemical complexity in the hot corinos around IRAS 16293 A and B (e.g. Cazaux et al. 2003; Bottinelli et al. 2004; Jaber et al. 2014; Jørgensen et al. 2016, 2018; Manigand et al. 2021; Müller et al. 2023, and references therein). On the other hand, the outer envelope is cold (~ 10 – 30 K), and characterized by the presence of small cyanopolynes (up to HC_5N , Jaber Al-Edhari et al. 2017), and small carbon chains such as $\text{c-C}_3\text{H}_2$, C_2H , C_3H , C_4H (Caux et al. 2011), primary revealed thanks to single-dish observations.

3 OBSERVATIONS

The observations were conducted on the GBT between June 2019 and February 2020, under project codes AGBT19A_048 and AGBT20A_135 (PI: C. Codella). The target sources, L1544 and IRAS 16293–2422, were observed at coordinates $\alpha_{J2000} = 05^h 04^m 16.6$ and $\delta_{J2000} = +25^\circ 10' 48.0''$, and $\alpha_{J2000} = 16^h 32^m 22.72$ and $\delta_{J2000} = -24^\circ 28' 34.3''$, respectively. Study of the cyanopolynes towards L1544 has already been presented in Bianchi et al. (2023). L1544 and IRAS 16293 were both observed with the Ku band receiver in combination with the VEGAS spectrometer in multiple set-ups to cover the frequency range (13.5 – 15.4 GHz). The resulting spectral windows had a bandwidth of 187.5 MHz and comprised 131,072 channels, yielding an extremely high spectral resolution of 1.4 kHz (equivalent to $\sim 50 \text{ m s}^{-1}$ and 30 m s^{-1} at 9 and 14 GHz, respectively). The spectral resolution of the IRAS 16293 spectrum was downgraded to 2.98 kHz for $\text{c-C}_3\text{H}$, C_6H , and HC_9N , while a resolution of 24 kHz was used for HC_7N to increase the S/N and identify weak lines. L1544 and IRAS16293 were observed for 6 and 8 hours, respectively. L1544 was successively observed in X band for additional 19 hours to cover the frequency range (8.0–11.6 GHz). The telescope’s half-power beam width (HPBW) ranged from approximately $54''$ in the Ku band to $84''$ in the X band. In L1544, the HNCO , methanol and $\text{c-C}_3\text{H}_2$ peaks, as reported in Lin et al. (2022), are included within the largest X beam. Pointing and focus were set using as calibrators the sources 1733-1304 and 0530+1331 for IRAS 16293 and L1544, respectively. The observations were carried out using position switching mode, employing an ON-OFF throw position of 1° west. Data reduction was performed using the GBTIDL software⁴. Initially, bad scans were identified and flagged, followed by the performance of ON-OFF position switching subtraction. The calibrated scans from each observing session were then noise-weighted averaged. Subsequently, any RFI (Radio Frequency Interference) and artifacts introduced by Doppler correction were identified and removed. A polynomial fit was applied to remove the baseline. Absolute flux calibration was then performed based on our flux calibrator observations, resulting in a calibration uncertainty of 20%. The typical root mean square (rms) noise level is $\sim 5 \text{ mK}$ per channel for both the Ku and X spectra. Line analysis was performed using the GILDAS⁵ CLASS package. Line intensities were converted to main beam temperature (T_{MB}) using the beam efficiencies of 0.9864 (10 GHz) and 0.959 (15 GHz), and forward efficiency >0.98 , reported in the GBT website¹.

⁴ <https://gbtidl.nrao.edu/>

⁵ <http://www.iram.fr/IRAMFR/GILDAS>

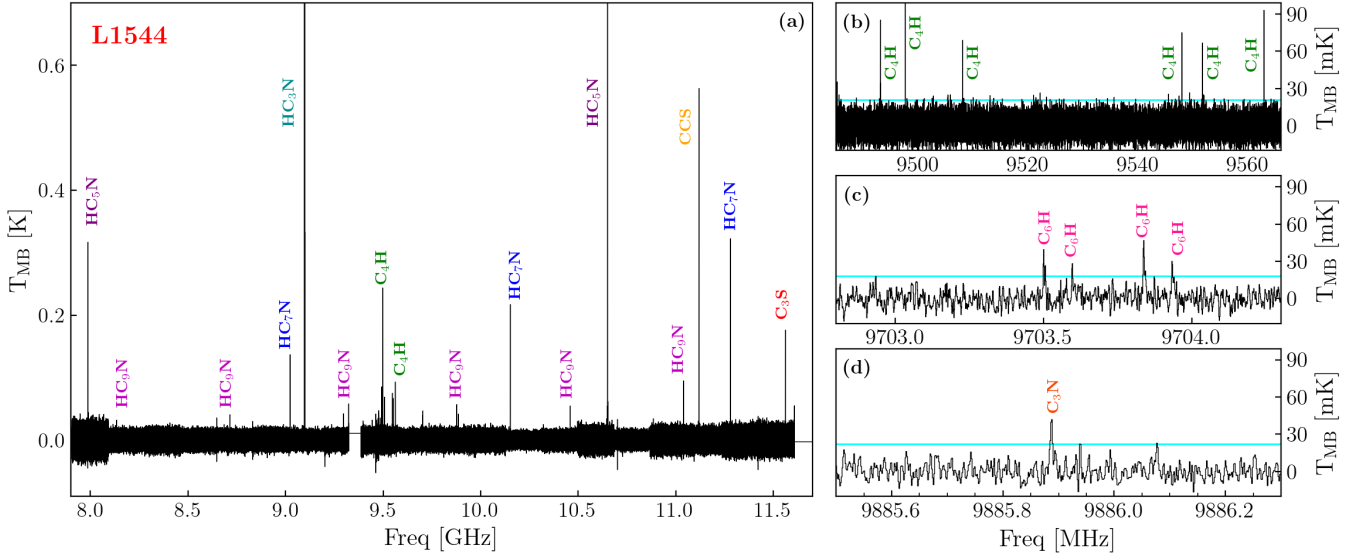


Figure 3. (Panel a): Full spectrum (in main-beam temperature, T_{MB}) of the L1544 prestellar source observed in X Band (7.8 – 11.6 GHz). The brightest lines associated with the detected species (see Tab. 1 for the list of all the detections) are labelled. The spectral resolution is 2.8 kHz ($\sim 60 \text{ m s}^{-1}$). (Panel b, c, d): Zooms in to highlight selected lines of C₄H, C₆H and C₃N, respectively. The cyan solid lines correspond to 3σ .

4 RESULTS

The spectra observed in Ku band for both L1544 and IRAS 16293, and that observed in X band towards L1544, are shown in Fig. 2 and 3, respectively. The present observations have revealed a significant number of complex carbon chain species, including C₂S, C₃S, C₃N, c-C₃H, C₄H, C₆H, HC₃N, HC₅N, HC₇N, and HC₉N. The lines are considered detected when the line peak intensity signal to noise (S/N) is at least 3. Table 1 reports the frequency of each transition (MHz), the energies of the upper level E_{up} (K), the line strength $S\mu^2$ (D²), the peak intensity T_{peak} in T_{MB} scale (mK) and the velocity integrated line intensity I_{int} (mK km s⁻¹). For L1544, we also include in Table 1 the cyanopolyyne lines previously published by Bianchi et al. (2023) from the same dataset. The most striking result from the Ku-band comparison (13.9–15.41 GHz), where both targets have been observed, is that L1544 exhibits a richer spectrum than the IRAS 16293 envelope (see Fig. 2). More specifically, in IRAS 16293 the only detected molecular species are c-C₃H and, in addition, ortho- and para- formaldehyde (H₂CO). Conversely, in L1544 we detected in Ku band, formaldehyde, c-C₃H, C₆H (with associated hyperfine structure), HC₇N, and HC₉N. In addition, the observations of L1544 performed in X band led to the detection of C₂S, C₃S, C₃N, C₄H, HC₅N, HC₅N and further lines of C₆H.

4.1 L1544

In L1544, we detected a single emission line from C₂S and C₃S, two lines from C₃N, eleven lines from c-C₃H, six lines from C₄H, and eight lines from C₆H (see Tab. 1). In addition, the HC₃N, HC₅N, HC₇N, and HC₉N lines detected in L1544 in the present dataset have been analysed in the study by Bianchi et al. (2023). The spectra of all the detected transitions for each species are shown in Figures 4, 5, 6 and 7. The exceptionally high spectral resolution of the present dataset ($\sim 50 \text{ m s}^{-1}$ and 30 m s^{-1} at 9 and 14 GHz, respectively; see Sect. 3) enables excellent sampling of the line profiles. All the detected species exhibit a double-peaked line profile, blue- and red-shifted by $0.1\text{--}0.2 \text{ km s}^{-1}$ with respect to the L1544 systemic velocity ($+7.2 \text{ km s}^{-1}$, e.g. Tafalla et al. 1998). The red-shifted peak has

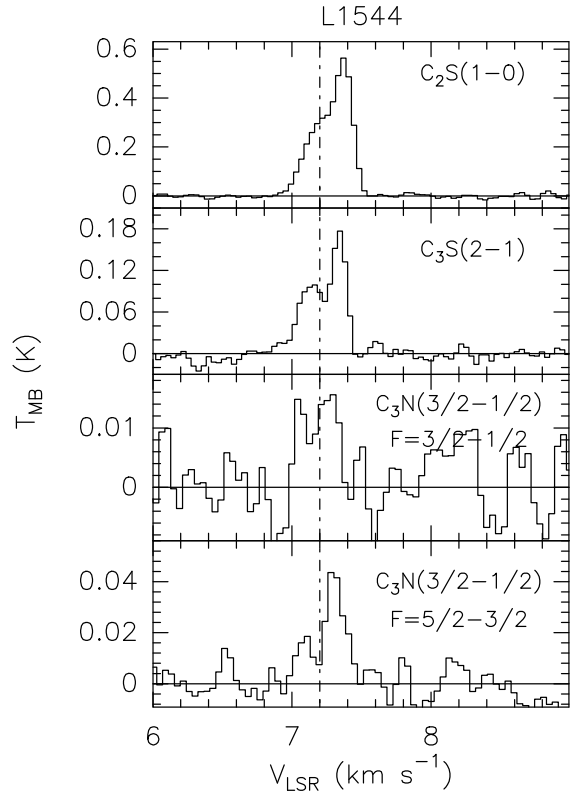


Figure 4. C₂S, C₃S, and C₃N spectra (in T_{MB} scale) observed towards L1544. The vertical dashed lines mark the ambient LSR velocity ($+7.2 \text{ km s}^{-1}$, Tafalla et al. 1998).

a higher intensity than the blue-shifted one. Moreover, the spectral profiles of the current dataset closely align with those previously observed in GBT K-Band toward L1544 for C₄H and C₆H, as reported by Gupta et al. (2009). This spectral characteristic profile has also been observed for cyanopolyynes (Bianchi et al. 2023), supporting

Table 1. Observed molecular lines towards L1544 and IRS16293. Line peak temperatures and velocity integrated intensities are in T_{MB} scale.

Species	Transition	ν^a (MHz)	E_{up}^a (K)	$S\mu^{2a}$ (D ²)	T_{peak}^b (mK)	I_{int}^b (mK km s ⁻¹)	T_{peak}^b (mK)		I_{int}^b (mK km s ⁻¹)
							L1544	IRAS 16293 ^c	
C ₂ S	N = 2–1, J=1–0	11119.446400(6E-7)	0.53	8.3	566±7	154±2
C ₃ S	J = 2–1	11561.513200(9E-7)	0.83	25.9	177±7	45±2
C ₃ N	N = 1–0 J=3/2–1/2 F = 3/2–1/2	9884.29320(1.6E-5)	0.47	5.6	16±6	4±1
C ₃ N	N = 1–0 J=3/2–1/2 F = 5/2–3/2	9885.89000(1.0E-5)	0.47	16.2	44±7	10±1
C ₃ N	N = 1–0 J=3/2–1/2 F = 3/2–3/2	9886.09420(2.7E-5)	0.47	5.2	≤ 15	≤ 3
C ₃ N	N = 1–0 J=3/2–1/2 F = 1/2–1/2	9886.99370(3.0E-5)	0.47	5.0	≤ 18	≤ 3
C ₃ N	N = 1–0 J=3/2–1/2 F = 1/2–3/2	9888.79480(3.5E-5)	0.47	0.4	≤ 21	≤ 4
C ₃ N	N = 1–0 J=1/2–1/2 F = 1/2–1/2	9911.18670(4.0E-5)	0.47	0.5	≤ 18	≤ 3
C ₃ N	N = 1–0 J=1/2–1/2 F = 1/2–3/2	9912.98770(3.6E-5)	0.47	5.0	≤ 18	≤ 3
C ₃ N	N = 1–0 J=1/2–1/2 F = 3/2–1/2	9913.64600(3.0E-5)	0.47	5.2	≤ 21	≤ 4
C ₃ N	N = 1–0 J=1/2–1/2 F = 3/2–3/2	9915.44700(1.6E-5)	0.47	5.6	≤ 21	≤ 4
c-C ₃ H	N = 1 _{1,0} –1 _{1,1} J=1/2–1/2 F = 1–1	14686.63000(4.0E-6)	0.71	3.8	71±7	23±1	21±4	13±2	
c-C ₃ H	N = 1 _{1,0} –1 _{1,1} J=1/2–1/2 F = 0–1	14689.71800(1.2E-5)	0.71	1.4	36±6	7±1	≤ 24	≤ 5	
c-C ₃ H	N = 1 _{1,0} –1 _{1,1} J=1/2–1/2 F = 1–0	14697.69200(8.0E-6)	0.71	2.6	46±7	14±2	≤ 24	≤ 5	
c-C ₃ H	N = 1 _{1,0} –1 _{1,1} J=1/2–3/2 F = 0–1	14755.39620(1.2E-5)	0.71	1.6	34±8	11±2	≤ 21	≤ 5	
c-C ₃ H	N = 1 _{1,0} –1 _{1,1} J=1/2–3/2 F = 1–2	14767.70000(8.0E-6)	0.71	2.8	66±7	15±2	15±5	11±1	
c-C ₃ H	N = 1 _{1,0} –1 _{1,1} J=1/2–3/2 F = 2–1	14812.01000(8.0E-6)	0.71	1.7	43±7	11±2	≤ 24	≤ 5	
c-C ₃ H	N = 1 _{1,0} –1 _{1,1} J=1/2–3/2 F = 1–1	14829.57100(6.4E-6)	0.71	2.0	43±8	12±2	≤ 24	≤ 5	
c-C ₃ H	N = 1 _{1,0} –1 _{1,1} J=1/2–3/2 F = 1–0	141(1.0E-5)	0.71	0.7	≤ 24	≤ 5	≤ 24	≤ 5	
c-C ₃ H	N = 1 _{1,0} –1 _{1,1} J=1/2–3/2 F = 2–1	14877.67500(4.0E-6)	0.71	2.0	41±6	12±2	≤ 24	≤ 5	
c-C ₃ H	N = 1 _{1,0} –1 _{1,1} J=3/2–3/2 F = 2–2	14893.05100(4.0E-6)	0.71	11.1	211±5	71±1	58±9	40±2	
c-C ₃ H	N = 1 _{1,0} –1 _{1,1} J=3/2–3/2 F = 1–1	14895.24300(8.0E-6)	0.72	5.3	104±5	71±1	27±3	14±2	
c-C ₃ H	N = 1 _{1,0} –1 _{1,1} J=3/2–3/2 F = 1–2	14910.62500(4.0E-6)	0.72	0.9	22±6	5±1	≤ 21	≤ 5	
C ₄ H	N = 1–0 J=3/2–1/2 F = 1–0	9493.06000(2.0E-6)	0.46	2.5	86±7	19±2	
C ₄ H	N = 1–0 J=3/2–1/2 F = 2–1	9497.61500(2.0E-6)	0.46	7.4	247±6	59±1	
C ₄ H	N = 1–0 J=3/2–1/2 F = 1–1	9508.00500(2.0E-6)	0.46	1.9	69±7	16±2	
C ₄ H	N = 1–0 J=1/2–1/2 F = 1–0	9547.96000(2.0E-6)	0.46	1.9	70±6	20±1	
C ₄ H	N = 1–0 J=1/2–1/2 F = 0–1	9551.72000(2.0E-6)	0.46	1.5	68±7	15±1	
C ₄ H	N = 1–0 J=1/2–1/2 F = 1–1	9562.90500(2.0E-6)	0.46	2.5	93±7	21±2	
C ₆ H	J=7/2–5/2 Ω=3/2 F=4–3 l=e	9703.5080(1.0E-2)	0.80	111.9	41±6	7±2	
C ₆ H	J=7/2–5/2 Ω=3/2 F=3–2 l=e	9703.6000(1.0E-2)	0.80	82.9	28±6	8±2	
C ₆ H	J=7/2–5/2 Ω=3/2 F=4–3 l=f	9703.8350(1.0E-2)	0.80	111.9	46±6	10±2	
C ₆ H	J=7/2–5/2 Ω=3/2 F=3–2 l=f	9703.9360(1.0E-2)	0.80	82.9	31±6	6±2	
C ₆ H	J=7/2–5/2 Ω=1/2 F=4–3 l=f	9758.8270(1.0E-2)	22.68	134.3	≤ 18	≤ 3	
C ₆ H	J=7/2–5/2 Ω=1/2 F=3–2 l=f	9759.1166(9.2E-3)	22.68	99.5	≤ 18	≤ 3	
C ₆ H	J=7/2–5/2 Ω=1/2 F=4–3 l=e	9786.7810(4.0E-3)	22.68	134.2	≤ 21	≤ 4	
C ₆ H	J=7/2–5/2 Ω=1/2 F=3–2 l=e	9787.0050(4.0E-3)	22.68	99.5	≤ 18	≤ 3	
C ₆ H	J=11/2–9/2 Ω=3/2 F=6–5 l=e	15248.2470(5.0E-3)	2.12	192.0	117±5	23±1	≤ 18	≤ 3	
C ₆ H	J=11/2–9/2 Ω=3/2 F=5–4 l=e	15248.3320(5.0E-3)	2.12	159.5	107±5	19±1	≤ 18	≤ 3	
C ₆ H	J=11/2–9/2 Ω=3/2 F=6–5 l=f	15249.0840(5.0E-3)	2.12	192.0	113±5	19±1	≤ 18	≤ 3	
C ₆ H	J=11/2–9/2 Ω=3/2 F=5–4 l=f	15249.1580(5.0E-3)	2.12	159.5	100±5	20±1	≤ 18	≤ 3	
C ₆ H	J=11/2–9/2 Ω=1/2 F=6–5 l=f	15343.1670(5.0E-3)	24.02	205.7	≤ 18	≤ 3	≤ 18	≤ 3	
C ₆ H	J=11/2–9/2 Ω=1/2 F=5–4 l=f	15343.2370(5.0E-3)	24.02	170.9	≤ 18	≤ 3	≤ 18	≤ 3	
C ₆ H	J=11/2–9/2 Ω=1/2 F=6–5 l=e	15371.5050(5.0E-3)	24.02	205.7	≤ 18	≤ 3	≤ 18	≤ 3	
C ₆ H	J=11/2–9/2 Ω=1/2 F=5–4 l=e	15371.5600(5.0E-3)	24.02	170.9	≤ 18	≤ 3	≤ 18	≤ 3	
HC ₇ N	J=13–12	14663.9937(2.0E-4)	4.93	906.1	443±7 ^d	151±1 ^d	9±2	9±2	
HC ₉ N	J=24–23	13944.8310(1.0E-3)	8.37	1947.0	152±6 ^d	24±1 ^d	≤ 18	≤ 2	
HC ₉ N	J=25–24	14525.8620(1.0E-3)	9.06	2028.1	157±6 ^d	25±1 ^d	≤ 15	≤ 2	
HC ₉ N	J=26–25	15106.8910(1.0E-3)	9.79	2108.9	166±6 ^d	26±1 ^d	≤ 15	≤ 2	

^a Frequencies and spectroscopic parameters have been provided by Yamamoto et al. (1990), Yamamoto et al. (1987), and Yamamoto & Saito (1994) for C₂S, C₃S, and c-C₃H, respectively, and extracted from the Jet Propulsion Laboratory molecular database (Pickett et al. 1998, and <https://spec.jpl.nasa.gov/>). On the other hand, frequencies and spectroscopic parameters for C₃N (Mikami et al. 1989), C₄H (Gottlieb et al. 1983), and C₆H (McCarthy et al. 1999; Gottlieb et al. 2010), are extracted from the Cologne Database for Molecular Spectroscopy (Endres et al. 2016; Müller et al. 2001, 2005, and <http://www.astro.uni-koeln.de/cdms/>). ^b Errors do not include 20% of calibration. Uncertainties on T_{peak} are the local rms of the spectra. Upper limits refer to the 3 σ level. Line integrated intensities (I_{int}) are computed by carefully selecting and integrating the emission over the relevant velocity range. ^c ‘...’ means that the frequency of the transition is not in the observed frequency range. ^d Data presented in Bianchi et al. (2023).

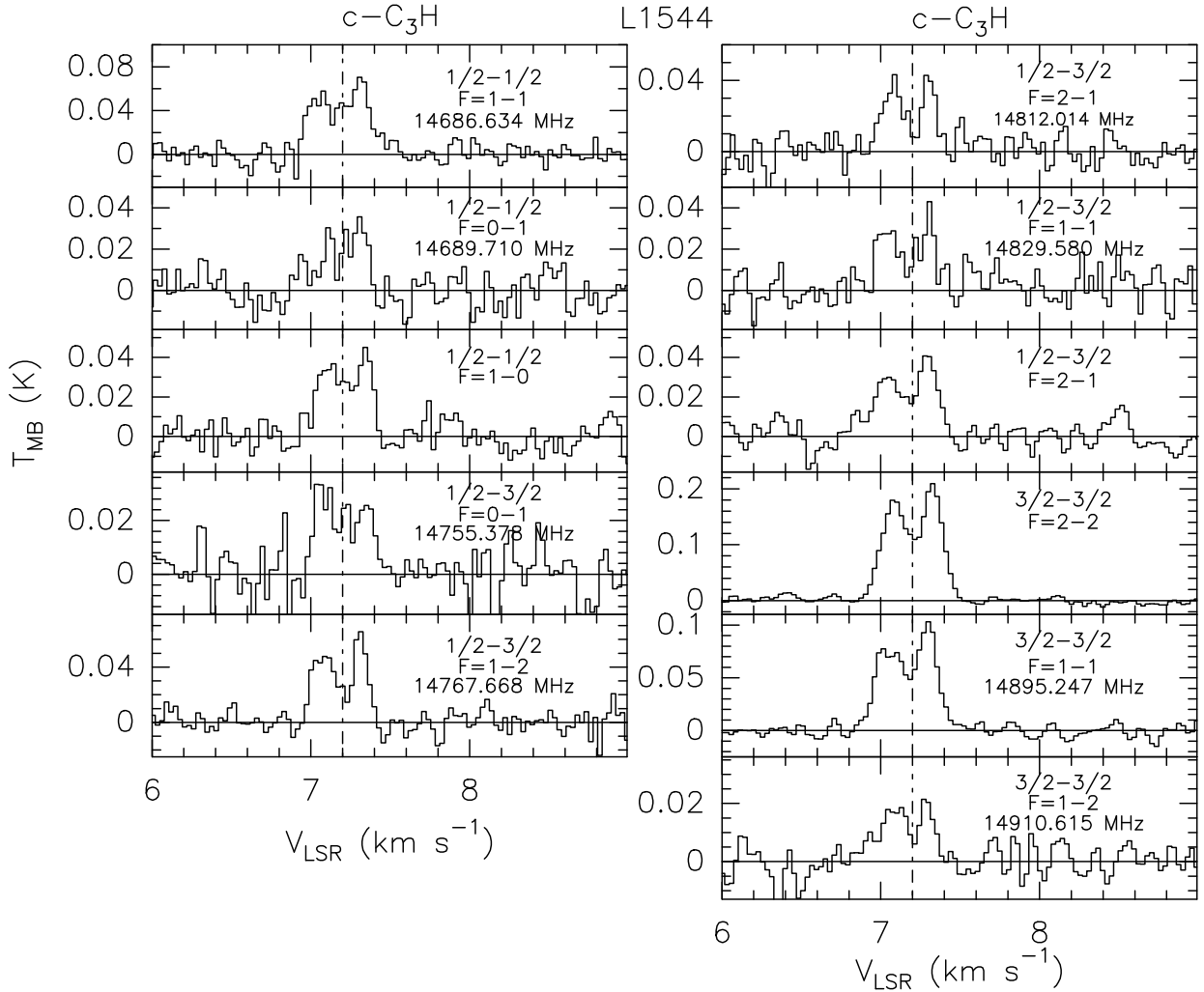


Figure 5. c-C₃H spectra (in T_{MB} scale) observed towards L1544. The vertical dashed lines mark the ambient LSR velocity (+7.2 km s⁻¹, Tafalla et al. 1998). When reported, the frequencies (in MHz) are different from those extracted from the JPL catalogue (Pickett et al. 1998), and refer to the values needed to center the spectra to the L1544 systemic velocity.

the idea that these molecules trace the same gas component. Given the asymmetric line profiles, we calculated the line-integrated intensities by carefully selecting and integrating the emission over the relevant velocity range. For non-detections, a 3σ upper limit on the integrated intensity (I_{int}) was estimated as $3\sqrt{N_{\text{ch}}}d\sigma$, where N_{ch} is the number of channels included in the integration (corresponding to a line width of 0.4 km s⁻¹, Bianchi et al. 2023) and $d\sigma$ is the velocity resolution. We included a calibration uncertainty of 20% in the calculation. To estimate the total column densities, N^{tot} , of the detected species, we used the integrated line intensities reported in Tab. 1. Given the absence of available collisional coefficients for c-C₃H and C₄H, and the detection of only a single line for C₂S, C₃S, C₃N and C₆H, we performed a Local Thermodynamic Equilibrium (LTE) analysis for these species. We assume that the emission fills the beam and we verify this assumption for C₆H, the only species having multiple detected transitions both in X- and Ku-band. In this case, the column densities derived using different transitions in X- and Ku-band independently are consistent within the uncertainties. We assume that the same is valid also for the other species. We derived column densities assuming excitation temperatures of both 5 K and 12 K, and we report the results as ranges of values. These lim-

its are consistent with the excitation temperatures found by Bianchi et al. (2023) for the cyanopolyyynes using the Large Velocity Gradient (LVG) method. Consequently, throughout this work we assume that the emission is optically thin and in LTE at the temperatures derived by Bianchi et al. (2023). For c-C₃H, C₄H and C₆H we used the hyperfine fitting method available in GILDAS to fit the hyperfine components to the available astronomical data. We confirm that emission is optically thin ($\tau < 0.1$) for all species, in agreement with what assumed in the present analysis. For C₂S, C₃S, C₃N and C₆H we calculate the critical density of the detected transition using the Einstein and collisional coefficients from the LAMDA database⁶ (Schöier et al. 2005), and from Walker et al. (2018), Sahnoun et al. (2020) and Lara-Moreno et al. (2021). For all species, we estimate $n_{\text{crit}} \lesssim 8 \times 10^3$ cm⁻³ at 10 K and $n_{\text{crit}} \lesssim 1 \times 10^4$ cm⁻³ at 20 K. In order to verify if the LTE assumption is valid, we consider the physical structure of the two sources. For L1544, the temperature is <12 K and the gas density is $\gtrsim 2 \times 10^4$ cm⁻³ within a radius of 7140 au probed by the GBT observations in X band, following the density profile by Keto & Caselli (2010). The same holds for IRAS 16293, where the density

⁶ <https://home.strw.leidenuniv.nl/moldata/>

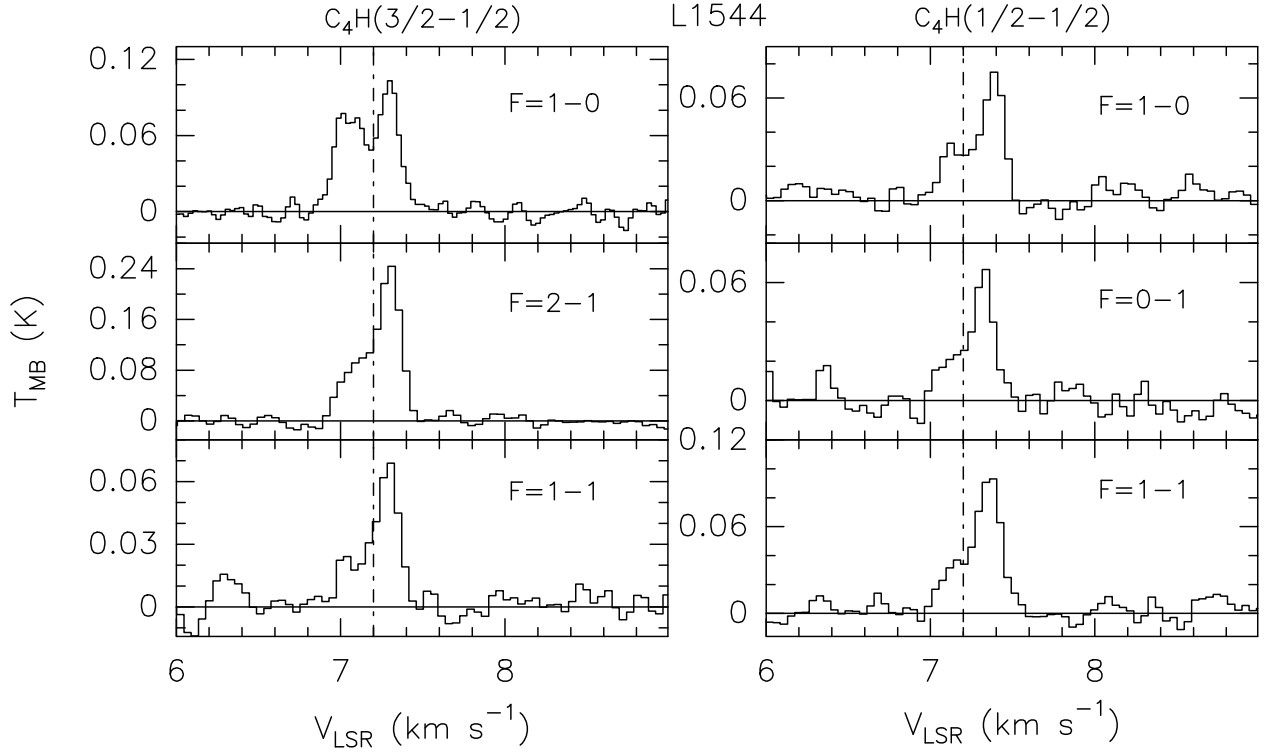


Figure 6. C_4H spectra (in T_{MB} scale) observed towards L1544. The vertical dashed lines mark the ambient LSR velocity ($+7.2 \text{ km s}^{-1}$, [Tafalla et al. 1998](#)).

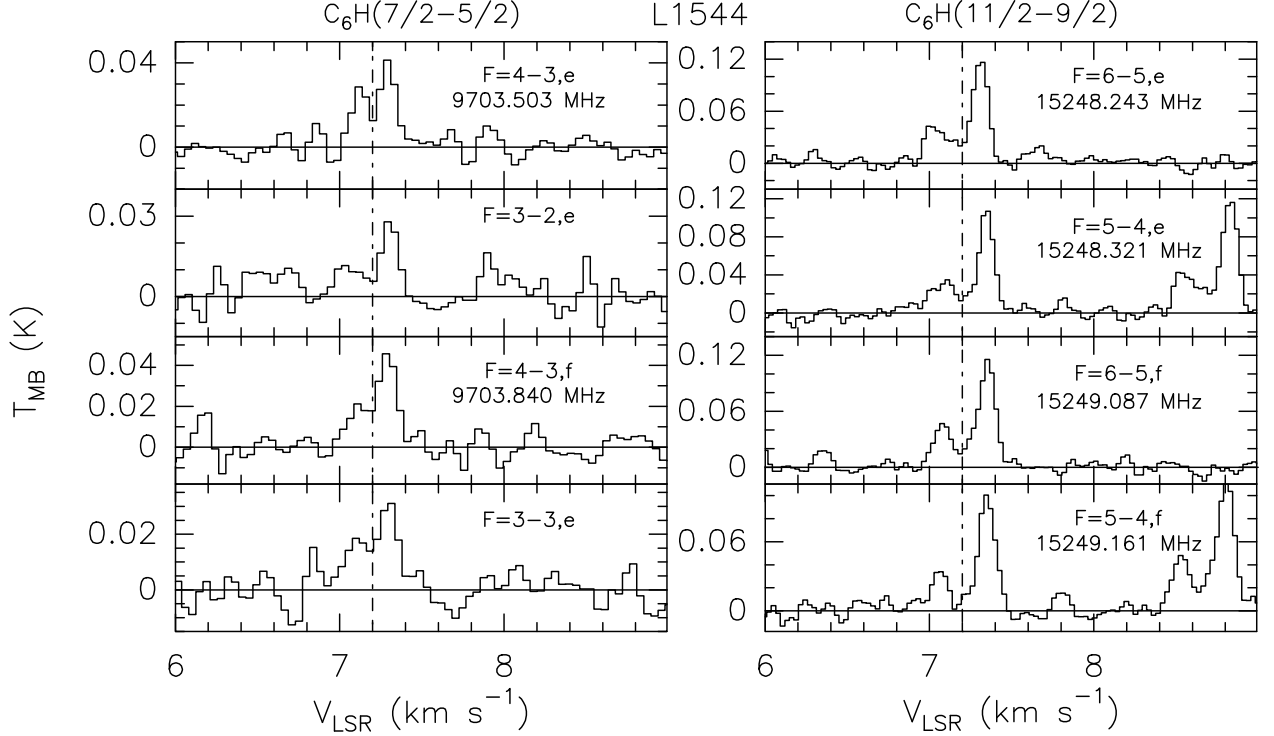


Figure 7. C_6H spectra (in T_{MB} scale) observed towards L1544. The vertical dashed lines mark the ambient LSR velocity ($+7.2 \text{ km s}^{-1}$, [Tafalla et al. 1998](#)). When reported, the frequencies (in MHz) are different from those extracted from the CDMS catalogue ([Müller et al. 2005](#)), and refer to the values needed to center the spectra to the L1544 systemic velocity.

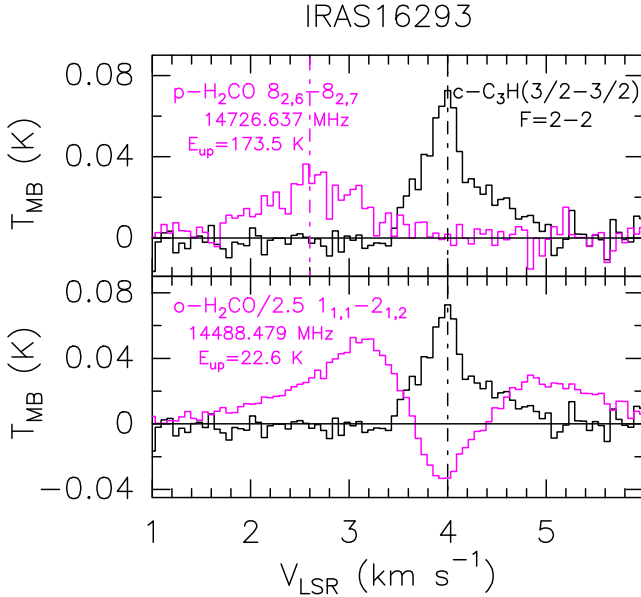


Figure 8. Upper panel: Comparison between the $c\text{-C}_3\text{H}(3/2-3/2)$ $F = 2-2$ (black) and $p\text{-H}_2\text{CO}(8_{2,6}-8_{2,7})$ ($E_{\text{up}} = 174$ K, magenta) line profiles observed towards IRAS 16293. The vertical scale is in T_{MB} units. The vertical dashed black line marks the LSR velocity of the envelope ($+4.0 \text{ km s}^{-1}$, Caux et al. 2011), while the magenta one is for the LSR velocity of the hot gas around the A and B protostars ($+2.6 \text{ km s}^{-1}$, Caux et al. 2011). Lower panel: Same as the upper panel using the low-excitation ($E_{\text{up}} = 23$ K) $o\text{-H}_2\text{CO}(1_{1,1}-2_{1,2})$ emission line (divided by a factor 2.5 for sake of clarity).

profile by Crimier et al. (2010) predicts a temperature of >15 K and gas densities $\gtrsim 4 \times 10^5 \text{ cm}^{-3}$ within a radius of 3807 au probed by the GBT observations in Ku band. For IRAS 16293 we also checked the critical densities for temperature higher than 20 K, which correspond to the inner regions. For $T > 20$ K, the gas density is larger than $1 \times 10^6 \text{ cm}^{-3}$, while critical densities are always lower than $5 \times 10^4 \text{ cm}^{-3}$. The LTE assumption is thus verified for the transitions of C_2S , C_3S , C_3N and C_6H . However, for other transitions from $c\text{-C}_3\text{H}$ and C_4H , collisional coefficients are not available. If the lines are sub-thermally populated, the column densities derived under the LTE assumption should be considered as lower limits.

4.1.1 The C_nX family: C_2S , C_3S , C_3N and $c\text{-C}_3\text{H}$

We detected C_2S ($N = 2-1$, $J = 1-0$) and $\text{C}_3\text{S}(2-1)$ (see Fig. 4), toward L1544. When considering the velocity-integrated emission and a temperature range between 5 and 12 K, we obtain $N_{\text{C}_2\text{S}}^{\text{tot}} = 1.1-2.0 \times 10^{13} \text{ cm}^{-2}$, and $N_{\text{C}_3\text{S}}^{\text{tot}} = 1.5-2.0 \times 10^{12} \text{ cm}^{-2}$. On the other hand, the C_3N ($3/2-1/2$) line (assuming again temperature in the 5–12 K range) leads to $N_{\text{C}_3\text{N}}^{\text{tot}} = 2-4 \times 10^{12} \text{ cm}^{-2}$. In all these cases, the column densities derived from the red-shifted peaks are $\sim 2-3$ times higher than those derived from the blue-shifted ones, consistent with the fact that the emission mainly originates from the southern region of L1544, as found for cyanopolyyynes by Spezzano et al. (2017) and Bianchi et al. (2023). The derived beam-averaged column densities are reported in Tab. 2. These values are consistent within a factor 3 with previous measurements obtained using the IRAM 30-m at 3 mm for C_2S , C_3S (Vastel et al. 2018b), and C_3N (Vastel et al. 2019).

For $c\text{-C}_3\text{H}$, we detect eleven hyperfine components corresponding to the $N=1_{1,0}-1_{1,1}$ transition (see Fig. 5), allowing us to derive $N_{\text{C}_3\text{H}}^{\text{tot}}$ between $2 \times 10^{12} \text{ cm}^{-2}$ (5 K), and $2 \times 10^{13} \text{ cm}^{-2}$ (12 K). These

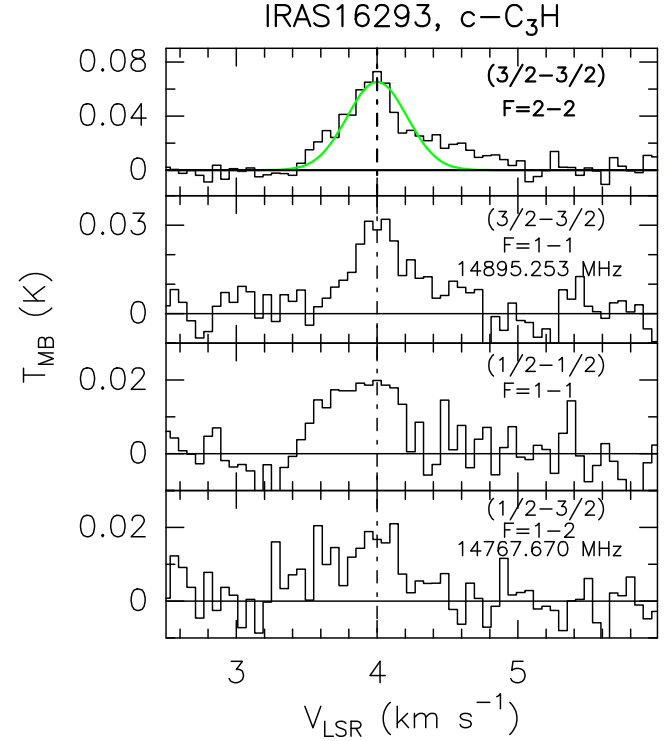


Figure 9. $c\text{-C}_3\text{H}$ spectra (in T_{MB} scale) observed towards IRAS 16293. The spectral resolution has been downgraded to 2.98 kHz ($\sim 60 \text{ m s}^{-1}$) to improve the S/N ratio. The green curve shows the envelope emission (see text). The vertical dashed lines mark the ambient LSR velocity ($+4.0 \text{ km s}^{-1}$, Caux et al. 2011). When reported, the frequencies (in MHz) are different from those extracted from the JPL catalogue (Pickett et al. 1998), and refer to the values needed to center the spectra to the IRAS 16293 systemic velocity.

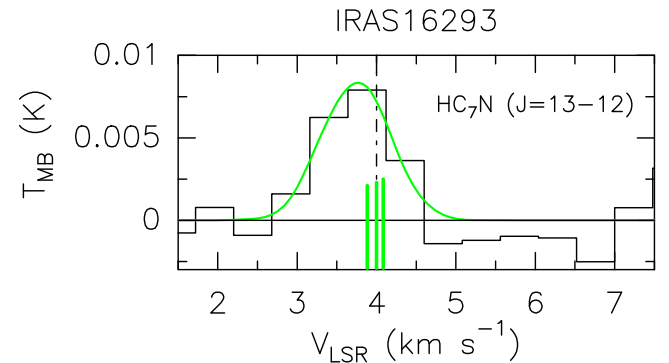


Figure 10. $\text{HC}_7\text{N}(13-12)$ spectra (in T_{MB} scale) detected towards IRAS 16293. The spectral resolution has been downgraded to 24 kHz ($\sim 0.5 \text{ km s}^{-1}$) to increase the S/N ratio. The vertical dashed line marks the ambient LSR velocity of the envelope ($+4.0 \text{ km s}^{-1}$, Caux et al. 2011). The green curve represents the Gaussian fit, while the vertical solid segments indicate the brightest hyperfine transitions ($F = 12-11$, $13-12$, and $14-13$, in order of increasing rest frequency) expected to contribute to the observed profile.

values are in agreement with those derived by (Mangum & Wootten 1990) at ~ 15 GHz using the GBT 100-m antenna.

4.1.2 The polyyynyl radicals family: C_4H and C_6H

We detected C_4H thanks to three hyperfine components of the $N = 1-0$ $J=3/2-1/2$ spectral pattern, as well as the $N = 1-0$ $J=1/2-1/2$ triplet

Table 2. Carbon chains column densities and abundances measured towards L1544 and IRAS 16293. The column densities are estimated assuming a gas temperature between 5 and 12 K in L1544 (Bianchi et al. 2023), and between 5 and 20 K in the envelope of IRAS 16293 (Jaber Al-Edhari et al. 2017), respectively. The abundances are derived assuming $N(H_2)$ of $2 \times 10^{22} \text{ cm}^{-2}$ for L1544 and $5 \times 10^{22} \text{ cm}^{-2}$ for IRAS 16293 (based on Herschel observations, see text).

Species	$N_{\text{tot}} (\times 10^{12} \text{ cm}^{-2})$		Abundances ($\times 10^{-10}$)		Reference
	L1544	IRAS 16293	L1544	IRAS 16293	
C_2S	11–20	–	5.5–10.0	–	1
C_3S	1.5–2.0	–	0.7–1.0	–	1
C_3N	2.0–3.6	–	1.0–1.8	–	1
$\text{c-C}_3\text{H}$	2.4–17.8	1.4–8.9	1.2–8.9	0.3–1.8	1
C_4H	13.7–30.9	–	6.8–15.5	–	1
C_6H	0.58–1.79	≤ 0.1 –0.5	0.3–0.9	< 0.02–0.1	1
HC_3N	> 80	–	> 40	–	2
HC_5N	30–200	–	15–100	–	2
HC_7N	4–50	0.06–0.11	2–25	0.012–0.022	1,2
HC_9N	0.8–16.0	≤ 0.029 –0.032	0.4–8.0	< 0.0058–0.064	1,2

[1] This work; [2] Bianchi et al. 2023

(see Fig. 6). C_6H is detected in both X and Ku bands (see Fig. 7). Specifically, four hyperfine components of the $J=7/2-5/2$ transition with upper level energy of 0.80 K are detected in X band (~ 9 GHz), while four hyperfine components of the $J=11/2-9/2$ transition with upper level energy of 2.1 K are detected in Ku band (~ 15 GHz). The line profiles of both C_4H , and C_6H show the characteristic double-peaked structure observed in L1544 using C_2S , C_3S , C_3N and $\text{c-C}_3\text{H}$ (Sec. 4.1), and cyanopolyynes (Bianchi et al. 2023), with the red-shifted peak brighter (by a factor ~ 2) than the blue-shifted one.

From the LTE analysis of the velocity-integrated emission, we derived $N_{\text{C}_4\text{H}}^{\text{tot}} = 1 \times 10^{13} \text{ cm}^{-2}$ and $3 \times 10^{13} \text{ cm}^{-2}$ for temperatures of 5 K and 12 K, respectively. On the other hand, $N_{\text{C}_6\text{H}}^{\text{tot}}$ is $0.58\text{--}1.79 \times 10^{12} \text{ cm}^{-2}$, adopting the 5–12 K range. These values are well consistent with previous GBT observations by Gupta et al. (2009). In contrast, our current measurement of the C_4H column density, derived using spectral parameters from the CDMS catalog (see Tab. 1), is an order of magnitude lower than that reported by Nagy et al. (2019) and Gupta et al. (2009), who presumably used the JPL catalog (Pickett et al. 1998). This discrepancy will be discussed in detail in Sect. 5.

4.2 IRAS 16293

The observations of IRAS 16293 show the detection of $\text{c-C}_3\text{H}$, H_2CO and HC_7N . The transitions of C_2S , C_3S , C_3N , and C_4H were not covered by the present observations. On the other hand, we provide upper limits for C_6H , and HC_9N . The $\text{c-C}_3\text{H}$ line peaks at approximately $+4 \text{ km s}^{-1}$, consistent with the systemic velocity of the IRAS 16293 envelope (Caux et al. 2011). The $\text{c-C}_3\text{H}$ and HC_7N transitions are single-peaked, associated with low upper level energies ($E_{\text{up}} < 25$ K) and the line profiles are narrow, with a $\text{FWHM} \leq 1 \text{ km s}^{-1}$. These findings support that the emission likely originates from the cold IRAS 16293 envelope, and not from the hot corino hosted inside the cloud. The high excitation ($E_{\text{up}} = 173.5$ K) $\text{p-H}_2\text{CO}(8_{2,6}-8_{2,7})$ transition peaks at around $+2.6 \text{ km s}^{-1}$, the systemic source velocity

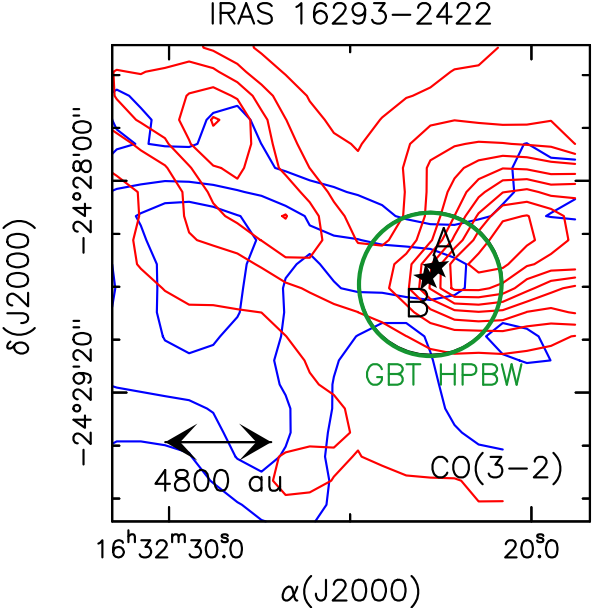


Figure 11. The red- and blue-shifted outflowing activity in the IRAS 16293 region as mapped by CO(3–2) using APEX observations adapted from Kahle et al. (2023). First steps and contours correspond to 3σ (2 K km s^{-1}) and 8σ , respectively. Black stars indicates the positions of the IRAS 16293 A and B protostars (e.g. Jørgensen et al. 2016). The green circle indicates the HPBW of the present GBT observations in the X band ($54''$).

of the IRAS 16293 B protostar (Caux et al. 2011). Conversely, the low-excitation $\text{o-H}_2\text{CO}(1_{1,1}-2_{1,2})$ line ($E_{\text{up}} = 23$ K) exhibits an absorption dip at the velocity of the envelope. This suggests absorption of the $\text{H}_2\text{CO}(1_{1,1}-2_{1,2})$ emission by the cold gas of the envelope. Figure 8 (upper panel) presents a comparison between the $\text{c-C}_3\text{H}(3/2-3/2) F = 2-2$ spectrum and the $\text{p-H}_2\text{CO}(8_{2,6}-8_{2,7})$ transition with $E_{\text{up}} = 174$ K. The differing peak velocities of these two spectral lines indicate emission originating from distinct physical components. For our subsequent analysis, we did not extend our investigation to H_2CO , owing to its unresolved components and extensive prior studies (e.g. van Dishoeck et al. 1995a; Ceccarelli et al. 2000; Loinard et al. 2000; van der Wiel et al. 2019). Instead, our focus was directed towards the emission of carbon chains from the cold envelope of IRAS 16293. The spectra of the detected $\text{c-C}_3\text{H}$ and HC_7N lines are reported in Figures 9 and 10. The spectral parameter of the observed lines, as well as the line integrated intensities used to calculate N^{tot} for each species, are reported in Tab 1. We calculate column densities for a temperature in the range 5–20 K following the results obtained by Jaber et al. (2014) from the analysis of cyanopolyynes in the envelope of IRAS 16293. The resulting N^{tot} are listed in Table 2. Note that, as for the L1544 case, the reported values are beam-averaged.

4.2.1 The C_nX family: $\text{c-C}_3\text{H}$

We detected four hyperfine components of the $N=1_{1,0}-1_{1,1}$ transition of $\text{c-C}_3\text{H}$ (see Fig. 9), with upper level energy (E_{up}) of 0.71 K. From the LTE analysis of the velocity-integrated emission of the two available brightest lines, we derived $N_{\text{c-C}_3\text{H}}^{\text{tot}} = 1.0\text{--}1.4 \times 10^{12} \text{ cm}^{-2}$, and $3.5\text{--}6.5 \times 10^{12} \text{ cm}^{-2}$, assuming a gas temperature between 5 and 20 K, respectively.

The line profile associated with the brightest $\text{c-C}_3\text{H}$ line ($J = 3/2-3/2 F = 2-2$) exhibits a red-shifted wing (up to $\sim 5 \text{ km s}^{-1}$). This is due to the fact that the GBT beam in X band ($54''$) encompasses

the bright and extended molecular outflow emerging from the protostellar system. Figure 11 shows the position of the GBT beam with respect the CO(3–2) outflow obtained using the Atacama Pathfinder Experiment (APEX, Güsten et al. 2006)⁷ telescope by Kahle et al. (2023). The present GBT observations sample a considerable part of the bright red-shifted lobe. This explains the red-shifted wing in the c-C₃H line ($J = 3/2$ to $3/2$ $F = 2-2$) spectrum, which is also consistent with the CO(3–2) spectrum extracted by Kahle et al. (2023) from the position of the red-shifted outflow peak.

We disentangled the contributions to the c-C₃H emission from the envelope and the outflow spectral wing by fitting the envelope with a gaussian profile and associating to the outflow the residual emission. We then derived their respective column densities. For the envelope, the integrated intensity is estimated using a Gaussian fit with FWHM of 0.5 km s^{-1} centered on the systemic velocity of $+4 \text{ km s}^{-1}$ (see Fig. 9). We obtained $N_{\text{tot}} = 1-4 \times 10^{12} \text{ cm}^{-2}$, assuming a gas temperature between 5 and 20 K. The residuals are used to estimate the outflow column density which is in the range $2-4 \times 10^{12} \text{ cm}^{-2}$, adopting a temperature range of 20–40 K (Jaber Al-Edhari et al. 2017; Kahle et al. 2023). For the outflow component, using the H₂ column density derived from the C¹⁷O column density of $1.9 \times 10^{15} \text{ cm}^{-2}$ measured by Kahle et al. (2023), assuming an isotopic ratio of $^{16}\text{O}/^{17}\text{O} = 2798$ (McKeegan et al. 2011), and a CO/H₂ abundance ratio of 2×10^{-4} , we obtained an estimate of the c-C₃H abundance with respect to H₂ of about 10^{-10} .

4.2.2 The polyyne radicals family: C₆H

Despite the presence of transitions in the Ku band, no C₆H lines were detected in the observed frequency range. Assuming a gas temperature between 5 and 20 K, we obtain an upper limit on the column density of $N_{\text{C}_6\text{H}} \leq 1-5 \times 10^{11} \text{ cm}^{-2}$ from the line at 15248.2470 MHz.

4.2.3 The cyanopolyyne family: HC₇N and HC₉N

Figure 10 shows that, once smoothed the spectral resolution to $\sim 0.5 \text{ km s}^{-1}$, we report, for the first time, the detection of HC₇N in IRAS 16293. The $J = 13-12$ transition was detected at 14.663 GHz with a S/N of 4σ (see Tab. 1). From an LTE analysis of the line, we derive a column density in the range $6-11 \times 10^{10} \text{ cm}^{-2}$, assuming a gas temperature between 5 and 20 K. We also derived an upper limit on the HC₉N column density of $N_{\text{HC}_9\text{N}} \leq 2.9-3.2 \times 10^{10} \text{ cm}^{-2}$ from the line at 15106.8910 MHz.

4.3 Suggested corrections for selected c-C₃H, and C₆H rest frequencies

In both L1544 and IRAS 16293 spectra, we detected several transitions of c-C₃H and C₆H at frequencies significantly offset from those reported in the spectroscopic databases, specifically, JPL for c-C₃H and CDMS for C₆H. Thanks to the high spectral resolution of the present observations (1.4 kHz), we were able to accurately determine the discrepancies between the observed frequencies (ν_{obs}) with the laboratory values reported in the spectral catalogues (ν_{spec}). Table 3 reports the observed frequencies for the c-C₃H, and C₆H transitions where the discrepancy is larger than twice the spectral resolution.

Note that, when observed in both L1544 and IRAS 16293, the frequency shifts are consistent, supporting the reliability of the corrections. We then propose these corrections in future updates of these databases. The corrected values for c-C₃H are in agreement with the recent laboratory measurements reported by Xue et al. (2025). For C₆H, we examined the new catalog reported by Remijan et al. (2023), and the transitions considered show the same frequency shifts as those found in our observations.

5 DISCUSSION

5.1 Comparison with previous observations

The L1544 prestellar core: L1544 has long been recognized as a chemically rich environment, particularly abundant in small carbon chains (C₂S, C₃S, C₃N, and c-C₃H), and cyanopolyyynes (e.g. Lin et al. 2022; Giers et al. 2022; Bianchi et al. 2023). The present GBT observations further enrich this picture, revealing carbon chains such as C₂S, C₃S, C₃N, and c-C₃H, along with the polyyne radicals C₄H and C₆H, which are known to be key precursors of cyanopolyyynes (Loison et al. 2014a; Giani et al. 2025). C₂S was first observed by Suzuki et al. (1992), with more recent estimates of the column density derived by Vastel et al. (2018b) and Nagy et al. (2019) using the IRAM 30-m telescope. Our derived column densities are systematically a factor of 2 higher, but remain in agreement with these studies within the associated uncertainty. This may suggest that the IRAM 30-m observations with telescope HPBW between 24'' and 30'', centered on the dusty peak of L1544, probably miss the extended emission which is instead recovered by the GBT beam. Indeed, our line profiles are consistent with the C₂S emission map reported by Spezzano et al. (2017), which shows an asymmetric distribution with enhanced emission in the south-east region of L1544. C₃S and C₃N detections were previously reported by Vastel et al. (2018b), and Vastel et al. (2019) using the IRAM 30-m antenna, finding column densities compatible (within a factor of 2) with the present ones.

The cyclic isomer c-C₃H was first detected in L1544 by Mangum & Wootten (1990) using the NRAO 43m telescope. In our dataset, only the cyclic form (c-C₃H) is detected and not the linear one (l-C₃H). Loison et al. (2017) analyzed the chemistry of c- and l-C₃H in dark clouds (TMC-1 and B1-b), reporting typical c/l abundance ratios of ~ 5 . Thanks to calculations of rovibrational density of states, they showed that, when formed in highly excited states, the isomerization between the cyclic and linear isomers (i.e. c-C₃H \rightleftharpoons l-C₃H) favor the formation of the cyclic form. In addition, they found that the dissociative recombination (DR) of c,l-C₃H₂⁺ leads mainly to cyclic c-C₃H. Although the formation of c-C₃H is generally favored, the chemistry of the two isomers is tightly coupled. Given their common precursors and the ease of interconversion, c- and l-C₃H likely coexist and trace similar physical regions, and both should be considered in astrochemical modeling. As a matter of fact, our observed line profiles for c-C₃H are consistent with the l-C₃H map obtained by Spezzano et al. (2017) with the IRAM 30-m, revealing a more uniform distribution than C₄H and C₂S. The detection and analysis of cyanopolyyynes, up to HC₉N, in L1544 was previously reported by Bianchi et al. (2023), who derived abundance ratios of HC₅N:HC₇N:HC₉N = 1:0.16:0.25. C₄H and C₆H were previously observed in L1544 by Gupta et al. (2009) using GBT in the 18–22 GHz frequency range. Although our column density estimate for C₆H is consistent with their results, our value for C₄H is almost one order of magnitude lower, leading to a significantly higher C₆H/C₄H ratio (4–6% compared to 0.5–0.9%). This discrepancy arises because our

⁷ <https://www.apex-telescope.org>

Table 3. List of the transitions observed at frequencies (ν_{obs}) different from those listed in the spectral catalogues (ν_{spec}), listed in Table 1. The uncertainties on the observed frequencies are assumed to be twice the spectral resolution of the GBT backend, i.e. 2.8 kHz.

Species	Transition	L1544		IRAS 16293	
		$\nu_{\text{obs}}^{\text{a}}$ (MHz)	$\nu_{\text{obs}} - \nu_{\text{spec}}$ (kHz)	ν_{obs} (MHz)	$\nu_{\text{obs}} - \nu_{\text{spec}}$ (kHz)
c-C ₃ H	N = 1 _{1,0} –1 _{1,1} J=1/2–1/2 F = 1-1	14686.634	+4	-	-
c-C ₃ H	N = 1 _{1,0} –1 _{1,1} J=1/2–1/2 F = 0-1	14689.710	-8	-	-
c-C ₃ H	N = 1 _{1,0} –1 _{1,1} J=1/2–3/2 F = 0-1	14755.378	-18	-	-
c-C ₃ H	N = 1 _{1,0} –1 _{1,1} J=1/2–3/2 F = 1-2	14767.668	-32	14767.670	-30
c-C ₃ H	N = 1 _{1,0} –1 _{1,1} J=1/2–3/2 F = 2-1	14812.014	+4	-	-
c-C ₃ H	N = 1 _{1,0} –1 _{1,1} J=1/2–3/2 F = 1-1	14829.580	+9	-	-
c-C ₃ H	N = 1 _{1,0} –1 _{1,1} J=3/2–3/2 F = 1-1	14895.247	+4	14895.253	+10
c-C ₃ H	N = 1 _{1,0} –1 _{1,1} J=3/2–3/2 F = 1-2	14910.615	-10	-	-
C ₆ H	J=7/2–5/2 Ω =3/2 F=4–3 l=e	9703.503	-5	-	-
C ₆ H	J=7/2–5/2 Ω =3/2 F=4–3 l=f	9703.840	+5	-	-
C ₆ H	J=11/2–9/2 Ω =3/2 F=6–5 l=e	15248.243	-4	-	-
C ₆ H	J=11/2–9/2 Ω =3/2 F=5–4 l=e	15248.321	-11	-	-
C ₆ H	J=11/2–9/2 Ω =3/2 F=6–5 l=f	15249.087	+3	-	-
C ₆ H	J=11/2–9/2 Ω =3/2 F=5–4 l=f	15249.161	+3	-	-

^a The observed frequencies were derived from the spectra at the native spectral resolution of 1.4 kHz.

analysis adopts the revised dipole moment for C₄H from [Oyama et al. \(2020\)](#), which is 2.4 times higher than the earlier value (2.1 D vs. 0.9 D) listed in the JPL and CDMS spectral databases. This leads to C₄H abundances that are a factor of 5.44 lower than previous estimates, resulting in proportionally higher C₆H/C₄H ratios.

The IRAS 16293 protostellar system: IRAS 16293 has been a subject of extensive investigations, with studies focusing on both its cold envelope (e.g. [Blake et al. 1994](#); [van Dishoeck et al. 1995a](#); [Caux et al. 2011](#)) and the protostellar system (e.g. [Jørgensen et al. 2016, 2018](#)). The narrow linewidths (FWHM $\leq 1 \text{ km s}^{-1}$) and low upper level energies of the molecular lines observed with this study, as well as the analysis of H₂CO lines, confirm that the detected emission predominantly arises from cold envelope gas, with minor contamination from the red-shifted outflow (e.g., in c-C₃H; see Sec. 4.2 and Fig. 9). Our observations allow for the first detection of HC₇N towards IRAS 16293. We also report, for the first time, upper limits for C₆H and HC₉N. Previous detections of c-C₃H and C₄H were reported by [Caux et al. \(2011\)](#). The emission is confirmed to originate from the cold envelope due to its narrow line profiles; however, no column density was derived. Emission from C₄H have been reported also by [Sakai et al. \(2009\)](#) and [Lindberg et al. \(2016\)](#), using the Mopra 22-m and the Kitt Peak 12-m telescopes, respectively. Based on the C₄H column density from [Lindberg et al. \(2016\)](#) and the C₆H column density derived in this work, we derive a C₆H/C₄H ratio of approximately 0.05, consistent with values observed in other sources (see Sec. 5.2 and 5.3).

Beside the upper limit on CCS column density, $N^{\text{tot}} \leq 1 \times 10^{15} \text{ cm}^{-2}$, set by [van Dishoeck et al. \(1995b\)](#) using the CSO 1.4-m and JCMT 15-m antennas, and $N^{\text{tot}} \leq 4 \times 10^{13} \text{ cm}^{-2}$ reported by [Drozdovskaya et al. \(2018\)](#) with ALMA in the IRAS 16293 B hot corino, no additional observational data are available for CCS, C₃S, or C₃N in the IRAS 16293 envelope for a direct comparison with the present dataset.

HC₃N has previously been detected (i) toward protostars using SMA, VLA, and ALMA interferometers by [Kuan et al. \(2004\)](#), [Chan-](#)

[dler et al. \(2005\)](#), and [Calcutt et al. \(2018\)](#), respectively, and (ii) sampling large spatial scales by [van Dishoeck et al. \(1995b\)](#) using JCMT 15m (beam size 20'') and [Jaber Al-Edhari et al. \(2017\)](#) using IRAM 30-m (beam size 30''). [van Dishoeck et al. \(1995b\)](#) observed three high-excitation transitions (28–27, 27–26, and 26–25), deriving a rotational temperature of $\sim 115 \text{ K}$ and a column density of $N_{\text{HC}_3\text{N}}^{\text{tot}} = 2\text{--}5 \times 10^{12} \text{ cm}^{-2}$. In contrast, [Jaber Al-Edhari et al. \(2017\)](#) observed 15 transitions in addition to the three lines reported by [van Dishoeck et al. \(1995b\)](#), covering also transitions from (9–8) up to (30–29). Based on these data, they derived an excitation temperature of 20 K and a column density of $N_{\text{HC}_3\text{N}}^{\text{tot}} = 3.2\text{--}5.6 \times 10^{11} \text{ cm}^{-2}$ for the outer envelope. Since the high-excitation lines detected by [van Dishoeck et al. \(1995b\)](#) are not expected to arise from the cold envelope, we adopt the values reported by [Jaber Al-Edhari et al. \(2017\)](#) for the outer envelope in the following analysis. In addition, [Jaber Al-Edhari et al. \(2017\)](#) also reported the detection of HC₅N in the envelope of IRAS 16293, deriving a column density of $N_{\text{HC}_5\text{N}}^{\text{tot}} = 3.6\text{--}7 \times 10^{11} \text{ cm}^{-2}$ at 20 K. The HC₇N column density derived in this work is consistent with the upper limit ($N \leq 5.3 \times 10^{13} \text{ cm}^{-2}$) derived by [Jaber Al-Edhari et al. \(2017\)](#). This implies no significant beam dilution differences are observed between GBT and IRAM 30-m data, implying an extended emitting region, larger than both telescope beams. The inferred HC₅N:HC₇N:HC₉N ratios in the IRAS 16293 envelope is 1:0.14:<0.28, closely matching those derived for L1544 ([Bianchi et al. 2023](#)), suggesting similar cyanopolyynes chemistry across different cold environments.

5.2 Comparison between prestellar core and protostellar envelope chemistry

To investigate the chemical differentiation between L1544 and IRAS 16293, we compared the column densities of carbon chains and cyanopolyynes in the two sources (Fig. 12). The comparison reveals several key points:

- (i) Cyanopolyynes exhibit similar relative column density ratios

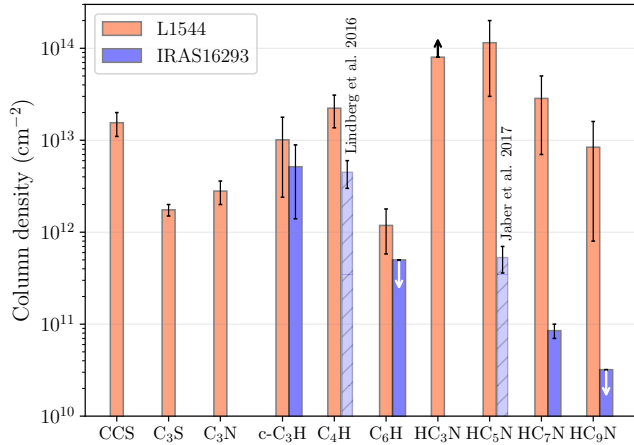


Figure 12. Column densities of carbon chains and cyanopolyyynes (see Tab. 2) observed in L1544 (orange bars) and IRAS 16293 (blue bars). The upper limits on C₆H and HC₉N column densities in L1544 are shown with white arrows. The black arrow is for the lower limit on the HC₃N column density due to opacity effects (Bianchi et al. 2023). The C₄H and HC₅N values in IRAS 16293 are taken from Lindberg et al. (2016) and Jaber Al-Edhari et al. (2017), respectively.

in both sources (HC₅N:HC₇N:HC₉N = 1:0.16:0.25 in L1544 and 1:0.14:<0.28 in IRAS 16293) yet their absolute column densities are systematically lower in IRAS 16293, possibly related to a chemical difference between the cold molecular envelope of IRAS 16293 and L1544;

- (ii) A similar trend is observed for the polyyynyl radicals (e.g., C₄H, C₆H), consistent with their role as precursors of cyanopolyyynes;
- (iii) c-C₃H is the only species with comparable column densities in both sources, within uncertainties;
- (iv) No detections of C₂S, C₃S, or C₃N are available in the literature for the IRAS 16293 envelope, preventing a direct comparison for these species.

In Figure 13 we compare the column densities of polyyynyl radicals C_{2n}H and cyanopolyyynes HC_{2n+1}N measured in different star forming regions. The figure shows that, using the updated C₄H spectral values, a clear exponential decrease in the column densities of polyyynyl radicals is revealed. A similar, though shallower, trend is observed for cyanopolyyynes, supporting a chemical connection between the C_{2n}H and HC_{2n+1}N families. Unsaturated carbon chains are believed to form mainly through neutral-neutral and ion-neutral reactions in the gas phase. Formation on grain surfaces is unlikely due to rapid hydrogenation by accreting H atoms (Hiraoka et al. 2000; Kobayashi et al. 2017; Molpeceres & Rivilla 2022; Fedoseev et al. 2025; Raaphorst et al. 2025). Giani et al. (2025) revised the neutral-neutral reactions of formation of HC₅N and found that in cold environments (T~10 K) reactions such as C₆H + N, C₃N + C₂H₂, and HC₃N + C₂H are the dominant ones. The observed exponential decrease in the abundances of polyyynyl radicals and cyanopolyyynes likely reflects a stepwise chemical growth, in which larger species derive from smaller precursors. For example, HC₅N may originate from HC₃N and C₆H, which themselves derive from smaller species such as C₄H. In general, the formation of carbon chains requires large amounts of atomic carbon. So far, two main scenarios have been proposed: either the gas is chemically young and carbon is not yet locked into CO, or a large irradiation by UV photons or cosmic rays drives CO dissociation, releasing carbon atoms into the gas phase (e.g., Agúndez & Wakelam 2013; Sakai & Yamamoto 2013; Spez-

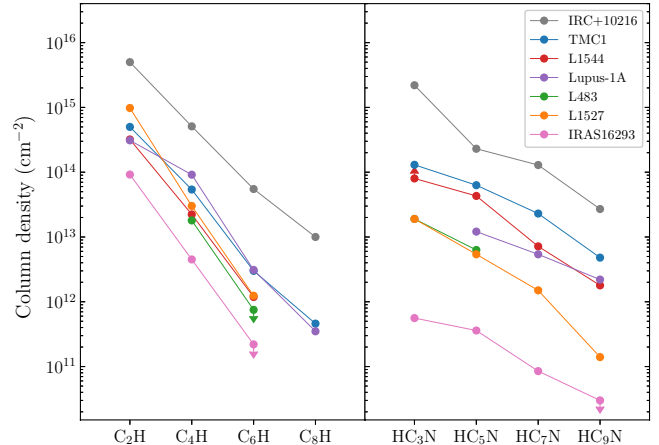


Figure 13. Comparison between column densities of polyyynyl radicals C_{2n}H (Left panel) and cyanopolyyynes HC_{2n+1}N (Right panel) measured in different star-forming regions. Values for L1544 are from the present work, and from Bianchi et al. (2023); Giers et al. (2023), while values for IRAS 16293 are from the present work, and from Jaber et al. (2014); Lindberg et al. (2016). Values for sources different than L1544, and IRAS 16293 are taken from Oyama et al. (2020, and references therein).

Table 4. Physical parameters and initial elemental abundances used in the cold prestellar core/envelope model. The upper half table lists the adopted parameters: H density, n_{H} , temperature, T, cosmic-ray ionisation rate, ζ_{CR} , visual extinction, A_{v} , dust grain radius, a_{d} , and grain density, ρ_{d} . The lower half table lists the initial elemental abundances relative to H nuclei, adapted from Jenkins (2009).

Physical parameters of the cold gas			
Parameter	Value	Parameter	Value
n_{H} [cm ⁻³]	2×10^4	A_{v} [mag]	1-10
T [K]	10	a_{d} [μm]	0.1
ζ_{CR} [s ⁻¹]	$0.1 - 10 \times 10^{-16}$	ρ_{d} [g cm ⁻³]	3

Initial elemental abundances (wrt H)			
Element	Abundance	Element	Abundance
H ₂	5.0×10^{-1}	Si ⁺	8.0×10^{-9}
He	9.0×10^{-2}	P ⁺	2.0×10^{-10}
C ⁺	2.0×10^{-5}	Na ⁺	2.0×10^{-9}
O	2.6×10^{-5}	Fe ⁺	3.0×10^{-9}
N	6.2×10^{-6}	Cl ⁺	1.0×10^{-9}
S ⁺	8.0×10^{-8}	F ⁺	1.0×10^{-9}

zano et al. 2016, 2017). Large values of $\zeta_{\text{CR}}(>10^{-16} \text{ s}^{-1})$ are however excluded by observations in L1544, as models better reproduces ions abundances when adopting $\zeta_{\text{CR}}=2-3 \times 10^{-17} \text{ s}^{-1}$ (Redaelli et al. 2021). To further explore the origin of the chemical differences between the two sources, we performed astrochemical modeling with varied physical parameters. The model description and results are presented in the following section.

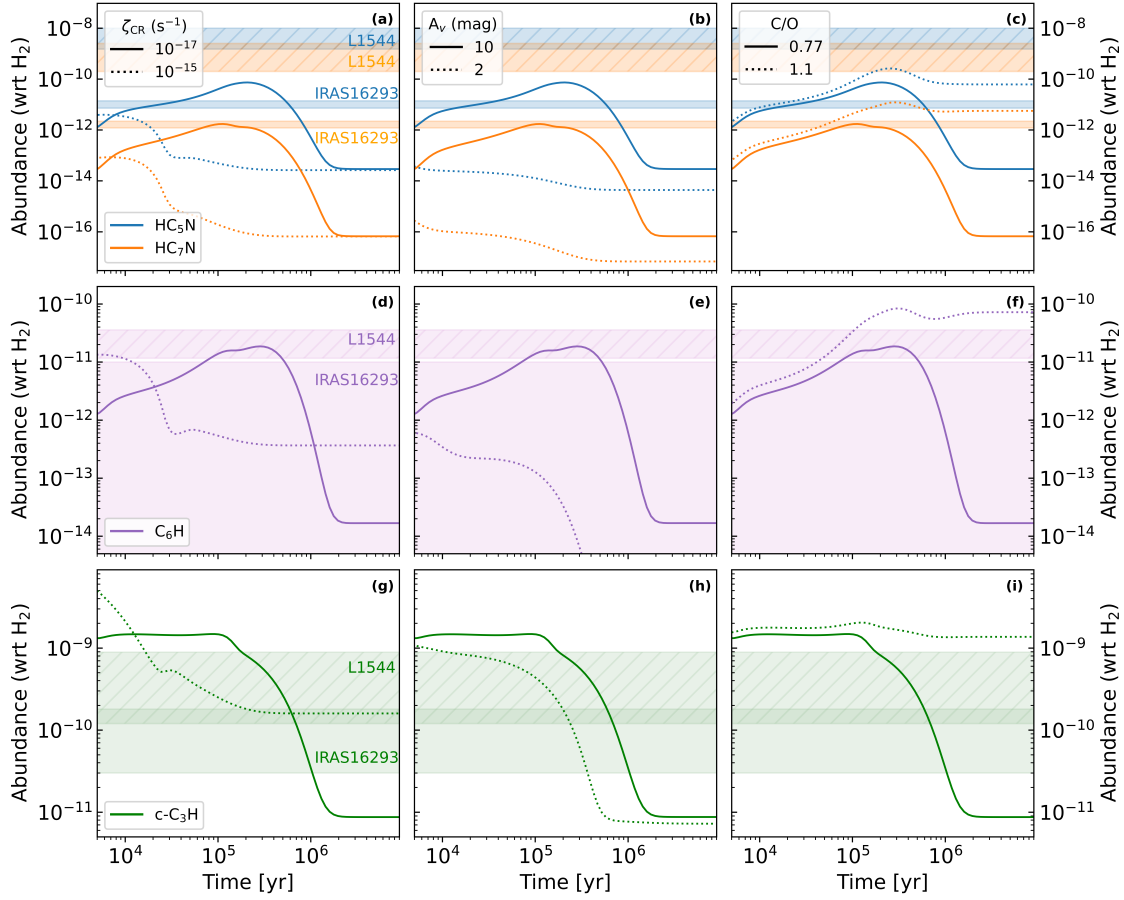


Figure 14. Comparison between the observed and modeled abundances of HC_5N , HC_7N , C_6H and $\text{c-C}_3\text{H}$ for different ζ_{CR} , A_v , and C/O ratios. Panels (a, b, c) show the predicted abundances of HC_5N (blue lines) and HC_7N (orange lines) as a function of the parameters indicated in the legends. Panels (d, e, f) and (g, h, i) show the same for C_6H (purple lines) and $\text{c-C}_3\text{H}$ (green lines), respectively. Observed values from L1544 and IRAS 16293 are shown as shaded bands, using the same color code as the model lines; dashed hatching indicates L1544. We assumed an $\text{N}(\text{H}_2)$ of $2 \times 10^{22} \text{ cm}^{-2}$ for L1544 and $5 \times 10^{22} \text{ cm}^{-2}$ for IRAS 16293 (based on Herschel observations, see text).

5.3 Astrochemical modeling

5.3.1 Model description

We ran the MyNahoon astrochemical model (Wakelam et al. 2005, 2010) to investigate the chemical diversity between L1544 and the cold molecular envelope of IRAS 16293. The model has been extensively described in previous works (Podio et al. 2014; Codella et al. 2017; Giani et al. 2023). In summary, it calculates the gas phase abundances of ~ 500 molecules as a function of time for some specific physical parameters, such as gas temperature, T , volume density, n_{H} , cosmic-ray ionization rate, ζ_{CR} , and visual extinction, A_v . We adopted the GRETOBAPE gas-phase reaction network (Tinacci et al. 2023), including recent updates on the chemistry of formation of HC_5N (Giani et al. 2025) and $\text{c-C}_3\text{H}$ (Loison et al. 2017). Surface chemistry (including adsorption and desorption) is not treated in the network, except for the formation of H_2 in dust grains. As unsaturated carbon chains are formed primarily in the gas phase, we do not expect a significant impact from the missing grain-surface processes. The initial elemental abundances and physical parameters adopted in the simulations are summarized in Tab. 4. To simulate the evolution of a typical translucent cloud into a molecular cloud, we assumed as initial conditions that elements with ionization potentials below 13.6 eV (e.g., C, S, Si, P) are ionized, while those

with higher values (N, O) are neutral. In all simulations, hydrogen is assumed to be fully molecular. The 0D model cannot capture the asymmetric spatial distributions of different species, likely arising from the source's physical structure (Jensen et al. 2023). However, we account for this limitation by comparing beam-averaged abundances with those predicted by the model. The key novelty of this model lies in the updated chemical network with thoroughly studied reaction rates, making it a valuable tool for exploring how the abundances of long carbon chains vary with different parameters. To assess the influence of cosmic rays and UV radiation on carbon chain formation, we ran a grid of models assuming the following ranges: (i) ζ_{CR} between $1 \times 10^{-17} \text{ s}^{-1}$ and $1 \times 10^{-15} \text{ s}^{-1}$ (Ceccarelli et al. 2014; Redaelli et al. 2021, 2025; Sabatini et al. 2023; Soccia et al. 2024); (ii) A_v between 1 and 10 mag. (iii) C/O elemental abundance ratios between 0.77 and 1.1. Since elemental depletion in the outer envelope of IRAS 16293 may not yet be complete, we also ran a model in which the initial elemental abundances from Tab. 4 were increased by a factor of 10. In order to compare the observed column densities with the abundances predicted by the model, we consider the H_2 column density to be at least $2 \times 10^{22} \text{ cm}^{-2}$ and $5 \times 10^{22} \text{ cm}^{-2}$ for L1544 and IRAS 16293, respectively, from Herschel observations (Kirk et al. 2013; Spezzano et al. 2016; Ladjelet et al. 2020) and in agreement with previous estimates (Crapsi et al. 2005;

van Dishoeck et al. 1995a). We note that these values correspond to the integrated H₂ column density along the line of sight, while the emission of carbon chains and cyanopolyynes may originate from an external layer, where the H₂ column density is likely lower. No direct measurements of H₂ in these region are available, making it difficult to accurately determine molecular abundances. To avoid assuming an arbitrarily reduced H₂ column density, we adopted the integrated values while emphasizing that the resulting abundances reported in Tab. 2 should be used with caution. Accordingly, in the discussion of the chemical modeling, we focus primarily on abundance ratios rather than absolute abundances.

5.3.2 Abundance of carbon chains

As a first test, we examined how variations in A_v, ζ_{CR} , and C/O elemental ratio affect the predicted abundances of carbon chains. For these models, we adopted the same gas density and temperature for L1544 and IRAS16293, given their similar physical conditions. Figure 14 compares the observed and modeled abundances of HC₅N, HC₇N, C₆H, and c-C₃H under these varying conditions. For both sources the best agreement with observations is obtained for cosmic-ray ionization rate $\zeta_{\text{CR}} = 1 \times 10^{-17} \text{ s}^{-1}$, visual extinction A_v=10 mag and C/O=0.77. In all models, cyanopolyyynes are underproduced by approximately two orders of magnitude compared to L1544 values. Conversely, good agreement is achieved for C₆H and c-C₃H abundances at times around $2\text{--}3 \times 10^5$ years. The recent revision of the gas-phase formation reactions of HC₅N by Giani et al. (2025) suggested that the C₆H + N reaction is the most important in cold regions. However, while the model considering this updated network correctly reproduces the C₆H abundance, it fails to reproduce that of HC₅N. If C₆H were indeed the major HC₅N precursor, the model should accurately predict HC₅N abundances. This discrepancy strongly suggests that additional formation reactions are missing from the chemical network, not only for HC₅N but also for the longer cyanopolyyynes. In IRAS 16293, the observed abundances of c-C₃H and HC₅N are well reproduced by the model at an age of approximately 7×10^5 years, in line with the source being more chemically evolved than L1544. At this time, however, the model underestimates the abundance of HC₇N by more than one order of magnitude. Unfortunately, the upper limit on the C₆H abundance is not sufficiently constraining for a meaningful comparison. When adopting less depleted initial elemental abundances, all species show comparable abundances at 10^5 years (with variations of less than one order of magnitude). At later times ($t > 10^6$ years), however, their abundances decrease by several orders of magnitude relative to the predictions obtained with the more depleted abundances, thereby worsening the agreement with the observations.

5.3.3 Abundance ratios of carbon chains

To overcome the substantial uncertainties associated with observed H₂ column densities, we also compare the model predictions with observed abundance ratios of the different species. Figure 15 shows the comparison of the predicted C₆H/C₄H ratios with those derived from observations, using both the old and revised dipole moment of C₄H. As discussed in Sec. 5.2, Oyama et al. (2020) estimated the C₄H dipole moment to be 2.4 times larger than the previous value, implying that previous estimates of its column density were overestimated by a factor of ~ 6 . When the corrected dipole moment is used, the observed C₆H/C₄H ratios, including those reported in this work, are in agreement with model predictions within a factor 3. This pos-

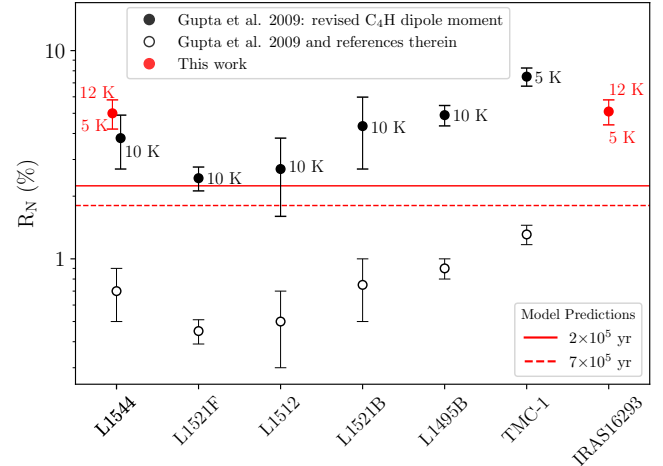


Figure 15. Comparison of the C₆H/C₄H ratio (R_N) obtained for L1544 with those derived in cold molecular clouds and protostars. Open circles correspond to data from Gupta et al. (2009, and references therein), while filled circles correspond to the same data corrected taking into account the revised dipole moment of C₄H (see text in Sec. 5 and Oyama et al. 2020). The R_N value derived in this work for L1544 and IRAS 16293 are shown in red. The temperatures at which the column densities of C₄H and C₆H have been derived are reported next to each point. R_N values predicted by the model at times of 2×10^5 and 7×10^5 years are shown as solid and dashed red lines, respectively. Model predictions are obtained assuming $\zeta_{\text{CR}} = 10^{-17} \text{ s}^{-1}$ and A_v=10 mag.

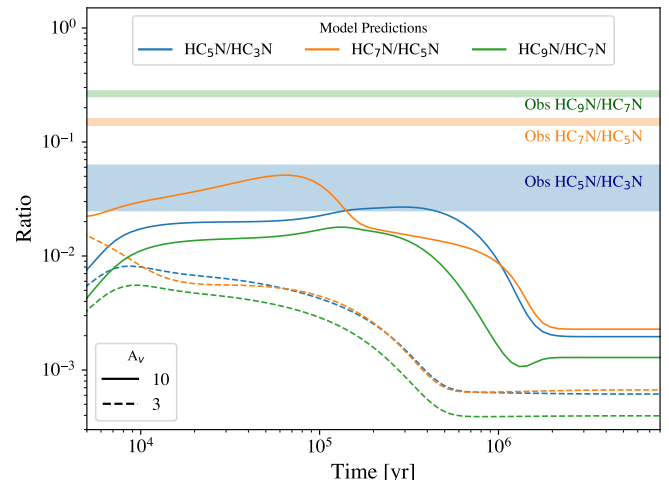


Figure 16. Comparison between predicted and observed abundance ratios of HC₅N/HC₃N, HC₇N/HC₅N, and HC₉N/HC₇N for different visual extinctions (A_v). Model predictions are shown as lines: blue for HC₅N/HC₃N, orange for HC₇N/HC₅N, and green for HC₉N/HC₇N. Solid lines correspond to A_v=10, while dashed lines to A_v=3. The observations, based on values derived for both L1544 and IRAS 16293 in this work, are represented as shaded bands in the same colors. Model predictions are obtained assuming $\zeta_{\text{CR}} = 10^{-17} \text{ s}^{-1}$ and A_v=10 mag.

sible discrepancy highlights the need for a revision of the formation and destruction pathways for these species.

Fig. 16 compares the predicted HC₅N/HC₃N, HC₇N/HC₅N and HC₉N/HC₇N ratios with those derived from the observations presented in this work. There is a clear discrepancy between models and observations with the exception of the HC₅N/HC₃N ratio,

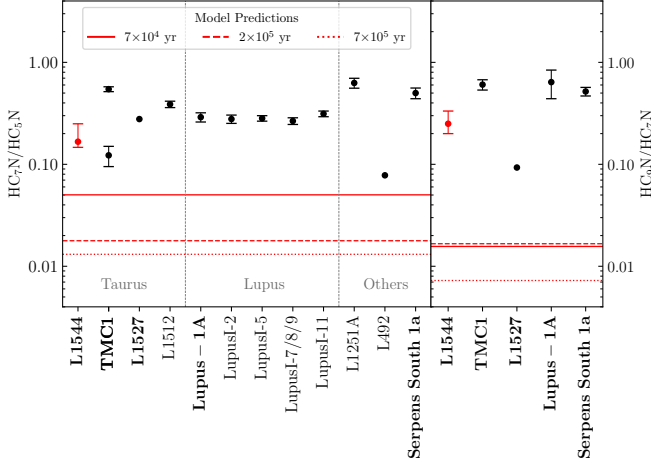


Figure 17. Comparison of the $\text{HC}_7\text{N}/\text{HC}_5\text{N}$ (Left panel), and $\text{HC}_9\text{N}/\text{HC}_7\text{N}$ (Right panel) ratios obtained for L1544 with those derived in cold molecular clouds. The values derived in this work for L1544 are shown as red circles. Values for L1544 are from the present work, while values for sources different than L1544 are taken from Bianchi et al. (2023, and references therein). Values predicted by the model at times of 7×10^4 , 2×10^5 and 7×10^5 years are shown as solid, dashed and dotted red lines, respectively. Model predictions are obtained assuming $\zeta_{\text{CR}} = 10^{-17} \text{ s}^{-1}$ and $A_v = 10$ mag. Sources for which both the $\text{HC}_7\text{N}/\text{HC}_5\text{N}$ and $\text{HC}_9\text{N}/\text{HC}_7\text{N}$ ratios are available are in boldface. Labels indicate the regions where sources are located: Taurus, Lupus, or other regions (Chameleon, Cepheus, and Aquila Rift).

which is reasonably reproduced at $t \sim 2-3 \times 10^5$ years with $A_v = 10$ mag. Figure 17 further illustrates that this discrepancy is not limited to a single source: even across different regions with different evolutionary ages, current models consistently underestimate the $\text{HC}_7\text{N}/\text{HC}_5\text{N}$ and $\text{HC}_9\text{N}/\text{HC}_7\text{N}$ ratios. Specifically, the predicted $\text{HC}_7\text{N}/\text{HC}_5\text{N}$ ratios are lower than observed by factors of $\sim 2-10$, while the $\text{HC}_9\text{N}/\text{HC}_7\text{N}$ ratios are underestimated by factors of $\sim 7-50$. Although existing models do reproduce the general trend of decreasing abundance with increasing molecular size, they fail to reproduce the observed abundance ratios, particularly for the longest chains. In order to explore the possibility that cyanopolyyynes and carbon chains arises from a UV illuminated region, as proposed by Spezzano et al. (2016) for L1544, we verified the impact of different A_v values on the model predictions. Fig. 18 shows the predicted abundances (with respect to H_2) of various carbon chains as a function of the visual extinction A_v . We conservatively assume a gas volume density $n_{\text{H}_2} = 10^4 \text{ cm}^{-3}$. Using the current network, cyanopolyyynes and polyynyl radicals show a strong decrease by 1 to 4 orders of magnitude from high to low A_v . In contrast, the abundance of c- C_3H remains nearly constant across the entire A_v range (between 1 and 10). Given that the major formation routes for cyanopolyyynes in the current chemical network are neutral-neutral reactions, it is not surprising that our model predicts a decrease in cyanopyyne abundance instead of an increase for higher UV illumination. On the contrary, the model successfully explains the presence of small carbon chains, such as c- C_3H and c- C_3H_2 , in highly irradiated environments (Favre et al. 2018). This suggests that additional formation reactions for cyanopolyyynes and their precursors are missing in the network. More specifically, additional ion-molecule reactions could explain the enhancement of cyanopolyyynes in UV exposed environments.

5.3.4 Observations vs models: carbon chains formation routes

Following the comparison of model predictions and observations reported in the previous sections, our main findings are:

(i) Models reproduce c- C_3H and C_6H in L1544 for $A_v = 10$, standard ζ_{CR} and C/O values, and times of $\sim 2-3 \times 10^5$ yr. For the same conditions, cyanopolyyynes are underproduced by a factor ~ 100 . For IRAS 16293, c- C_3H and HC_5N are reproduced by the model for $A_v = 10$ and times of $\sim 7 \times 10^5$ years, but not HC_7N .

(ii) Models reasonably reproduce the abundance ratios between species within the same chemical family for $A_v = 10$ and evolutionary timescales in the range $2-7 \times 10^5$ years. The $\text{C}_6\text{H}/\text{C}_4\text{H}$ and $\text{HC}_5\text{N}/\text{HC}_3\text{N}$ ratios are reproduced in both L1544 and IRAS 16293 (see Fig. 15 and 16), while the $\text{HC}_7\text{N}/\text{HC}_5\text{N}$ and $\text{HC}_9\text{N}/\text{HC}_7\text{N}$ ratios are underestimated by a factor of $\sim 2-50$ likely due to the incomplete chemical network for large cyanopolyyynes (see Fig. 17);

(iii) Cyanopolyyynes are predicted to be abundant in young objects, while their abundances decrease at later evolutionary stages ($t > 3 \times 10^5$ years; see Fig. 14). As proposed for the starless core TMC-1, this behavior can be explained by the larger availability of carbon atoms before being converted into CO (Agúndez & Wakelam 2013). This explains the higher cyanopyyne abundances observed in L1544 compared to IRAS 16293, since L1544 is a younger source.

(iv) Current models do not support the hypothesis that cyanopolyyne abundances are enhanced by elevated cosmic ray ionization rate or intense UV irradiation, despite indications from the asymmetric spatial distribution of carbon chains and cyanopolyyynes observed towards the southeastern region of L1544 (Spezzano et al. 2016; Bianchi et al. 2023). The discrepancy between predicted and observed abundances is particularly pronounced for cyanopolyyynes. This highlights the incompleteness of current chemical networks, especially regarding their formation reactions, which in turn impedes a comprehensive understanding of their primary formation mechanisms.

(v) Although previous studies have shown that neutral-neutral reactions are the primary formation routes of cyanopolyyynes (Giani et al. 2025), they cannot fully explain the observed abundances, especially in L1544. We therefore strongly suggest that additional ion-molecule reactions, beyond those currently included in the networks, are involved, as the production of ionic species can be enhanced in highly irradiated environments. A thorough revision of the formation pathways of the HC_5NH^+ ion, which could be a major precursor of HC_5N , is needed to verify this hypothesis (see Appendix for more details).

5.4 Future impact of SKA observations on carbon chain chemistry

The present observations confirm that complex carbon chemistry is already active from the earliest stages of Sun-like planetary system formation, with these species potentially contributing to the synthesis of molecules of prebiotic relevance. However, single-dish facilities have typically an angular resolution of $54''-84''$ in the 8-15 GHz range (corresponding to $\sim 10,000$ au scales for nearby star-forming regions), which allow for the observation of these species in extended sources, such as prestellar cores or protostellar envelopes, leaving it unclear whether they also exist at smaller angular scales. New possibilities to observe these species at high-angular resolution will be offered by

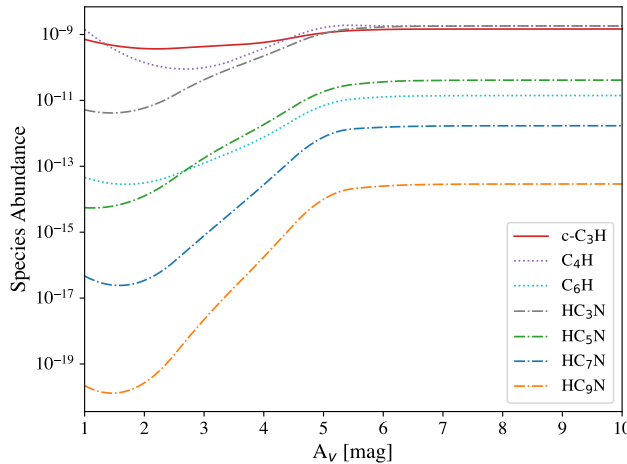


Figure 18. Predicted abundances (with respect to H₂) of c-C₃H (red solid line), C₄H (purple dotted line), C₆H (cyan dotted line), HC₃N (grey dashed line), HC₅N (green dashed line), HC₇N (blue dashed line), and HC₉N (orange dashed line) as a function of A_v. The model assumes n_{H₂}=10⁴ cm⁻³, T=10 K and $\zeta_{CR}=10^{-17}$ s⁻¹. The predictions refer to the model at 10⁵ yr.

next-generation facilities such as MeerKAT⁸ and the Square Kilometre Array Observatory (SKAO)⁹. Specifically, MeerKAT Band 5b (covering 8.3–15.4 GHz), currently under development, will enable observations of prestellar cores, protostellar envelopes, and protostellar shocks down to an angular resolution of a few hundreds au in the nearest star-forming regions. Subsequently, SKA-Mid Band 5 (covering the 4.6–15.4 GHz range) will allow for the exploration of this chemical complexity down to the 100 au scale within planet-forming regions. With these new facilities, multiple transitions of cyanopolyyynes up to HC₁₁N, and their precursors C₄H and C₆H, will be detectable in several sources, resolving emission both spatially and spectrally in just a few hours of observation for extended sources such as prestellar cores and protostellar shocks, and in 100–1000 hours for compact planet-forming disks. These future SKA observations, coupled with an exhaustive revision of the chemical reaction networks, will provide crucial new insights into the formation and destruction routes of these species and their possible role in promoting prebiotic chemistry.

6 CONCLUSIONS

In this paper, we report new observations of several carbon chains conducted with the 100-m GBT. These observations include Ku-band data (13.5–15.4 GHz) targeting both the L1544 prestellar core and the IRAS 16293 protostellar envelope, along with additional X-band data (8.0–11.6 GHz) towards L1544. The main results of the paper are:

- In L1544, we detect emission lines from C₂S, C₃S, C₃N, c-C₃H, C₄H and C₆H (with E_{up}≤2 K), in addition to those of HC₃N, HC₅N, HC₇N and HC₉N, already reported in Bianchi et al. (2023). All the lines have FWHM around 0.4 km s⁻¹ and show similar double-peaked profiles, suggesting a common underlying gas component.

- In IRAS 16293, we detect c-C₃H and, for the first time, HC₇N (emission lines with E_{up}≤5 K). We also report, for the first time, upper limits for C₆H and HC₉N. The detected lines have FWHM≤1 km

⁸ www.sarao.ac.za/science/meerkat/

⁹ www.skao.int/en

s⁻¹ and they arise from the cold envelope. For c-C₃H emission, we have contribution from both the cold envelope and the red-shifted outflow that we spectrally disentangle.

- We refine the spectroscopic frequencies of several c-C₃H and C₆H transitions, thanks to the high spectral resolution of the observations (1.4 kHz). The shifts between calculated and observed frequencies are consistent in both L1544 and IRAS 16293.

- We performed LTE analysis to derive column densities of the detected species, assuming gas temperatures in the range 5–12 K for L1544, and 5–20 K for IRAS 16293, respectively. All column density estimates obtained in this work are consistent with previous measurements, where available. The only exception is C₄H, for which we used the revised dipole moment reported by Oyama et al. (2020), that yields column densities lower by a factor ∼6 compared to previous estimates. In IRAS 16293 we also calculated, for the first time, the c-C₃H column density and abundance (∼10⁻¹⁰) in the outflow wing.

- IRAS 16293 is less rich in carbon chains compared to L1544, with all detected species (except for c-C₃H) showing column densities lower by a factor ∼10–100. Despite this difference, the ratios between polyyynyl radicals (C_{2n}H) and cyanopolyyynes (HC_{2n+1}N) are similar in both sources (i.e. C₄H:C₆H = 1:0.053 and HC₅N:HC₇N:HC₉N = 1:0.16:0.25 in L1544, and 1:0.048 and 1:0.14:<0.28 in IRAS 16293, respectively). When compared to other prestellar and protostellar sources at different evolutionary stages, cyanopolyyynes and polyyynyl radicals show the same exponentially decreasing trend, suggesting that their chemistry is likely the same across different cold environments.

- We used a gas-phase astrochemical model to reproduce the abundances and investigate the formation of carbon chains. The model employing A_v=10, standard ζ_{CR} , and typical C/O ratio reproduces the c-C₃H abundance in both sources, and the C₆H abundance in L1544. Conversely, while HC₅N is well reproduced in IRAS 16293, it is underestimated by more than an order of magnitude in L1544. The discrepancy is even more pronounced for HC₇N, whose abundance is systematically underpredicted by about two orders of magnitude in both sources.

- Models reproduce the C₆H/C₄H and HC₅N/HC₃N ratios in both L1544 and IRAS 16293 for A_v=10 and t=2–7×10⁵ years. However, the HC₇N/HC₅N and HC₉N/HC₇N ratios are systematically underestimated, likely due to incomplete chemical networks for large cyanopolyyynes.

This work paves the way for future astrochemical studies with next-generation radio interferometers such as SKAO. By enabling high-angular resolution observations of complex carbon-bearing molecules, these facilities will allow us to probe chemical complexity down to 100 au scales within star-forming regions. Combined with updated chemical reaction networks, such observations will provide critical insights into the formation of carbon chains and cyanopolyyynes and their prebiotic role.

ACKNOWLEDGEMENTS

We thank the anonymous referee for the instructive comments which improved the paper. The authors warmly acknowledge Angelique Kahle and Friedrich Wyrowski for providing the CO (3–2) APEX data. This project has received funding from the EC H2020 research and innovation programme for: (i) the project "Astro-Chemical Origins" (ACO, No 811312), and (ii) the European Research Council (ERC) project "The Dawn of Organic Chemistry" (DOC,

No 741002). CC, LP, and GS acknowledge the PRIN-MUR 2020 BEYOND-2p (Astrochemistry beyond the second period elements, Prot. 2020AFB3FX), the project ASI-Astrobiologia 2023 MIGLIORA (Modeling Chemical Complexity, F83C23000800005), the INAF-GO 2024 fundings ICES, and the INAF-GO 2023 fundings PROTO-SKA (Exploiting ALMA data to study planet forming disks: preparing the advent of SKA, C13C23000770005). LP, CC, and GS also acknowledge financial support under the National Recovery and Resilience Plan (NRRP), Mission 4, Component 2, Investment 1.1, Call for tender No. 104 published on 2.2.2022 by the Italian Ministry of University and Research (MUR), funded by the European Union – NextGenerationEU-Project Title 2022JC2Y93 Chemical Origins: linking the fossil composition of the Solar System with the chemistry of protoplanetary disks – CUP J53D23001600006 – Grant Assignment Decree No. 962 adopted on 30.06.2023 by the Italian Ministry of Ministry of University and Research (MUR). GS also acknowledges support from the INAF-Minigrant 2023 TRIESTE ("TRacing the chemical hEritage of our originsS: from protostars to planetEs"). EB acknowledges the support from the Italian Ministry for Universities and Research under the Italian Science Fund (FIS 2 Call - Ministerial Decree No. 1236 of 1 August 2023) and the Next Generation EU funds within the National Recovery and Resilience Plan (PNRR), Mission 4 - Education and Research, Component 2 - From Research to Business (M4C2), Investment Line 3.1 - Strengthening and creation of Research Infrastructures, Project IR0000034 – "STILES - Strengthening the Italian Leadership in ELT and SKA". The Green Bank Observatory is a facility of the National Science Foundation operated under cooperative agreement by Associated Universities, Inc. LG acknowledges support from the COST Action CA22133 PLANETS.

DATA AVAILABILITY

The data underlying this article are available in the NRAO archive at <https://data.nrao.edu/portal/#/>, and can be accessed with the project code.

REFERENCES

Agúndez M., Wakelam V., 2013, *Chemical Reviews*, **113**, 8710
 Agúndez M., et al., 2023, *A&A*, **673**, A34
 Andre P., Ward-Thompson D., Barsony M., 1993, *ApJ*, **406**, 122
 Balucani N., Ceccarelli C., Taquet V., 2015, Monthly Notices of the Royal Astronomical Society: Letters, **449**, L16
 Benson P. J., Myers P. C., 1989, *ApJS*, **71**, 89
 Bergin E. A., Tafalla M., 2007, *ARA&A*, **45**, 339
 Bianchi E., et al., 2023, *ApJ*, **944**, 208
 Bizzocchi L., Caselli P., Spezzano S., Leonardo E., 2014, *A&A*, **569**, A27
 Blake G. A., van Dishoeck E. F., Jansen D. J., Groesbeck T. D., Mundy L. G., 1994, *ApJ*, **428**, 680
 Blázquez S., et al., 2020, *Physical Chemistry Chemical Physics*, **22**, 20562
 Bottinelli S., et al., 2004, *ApJ*, **617**, L69
 Bouvier M., López-Sepulcre A., Ceccarelli C., Kahane C., Imai M., Sakai N., Yamamoto S., Dagdigian P. J., 2020, *A&A*, **636**, A19
 Bouvier M., Ceccarelli C., López-Sepulcre A., Sakai N., Yamamoto S., Yang Y.-L., 2022, *ApJ*, **929**, 10
 Burkhardt A. M., Loomis R. A., Shingledecker C. N., Lee K. L. K., Remijan A. J., McCarthy M. C., McGuire B. A., 2021, *Nature Astronomy*, **5**, 181
 Calcutt H., et al., 2018, *A&A*, **616**, A90
 Caselli P., Ceccarelli C., 2012, *A&ARv*, **20**, 56
 Caselli P., Walmsley C. M., Tafalla M., Dore L., Myers P. C., 1999, *ApJ*, **523**, L165
 Caselli P., et al., 2022, *ApJ*, **929**, 13
 Castets A., Ceccarelli C., Loinard L., Caux E., Lefloch B., 2001, *A&A*, **375**, 40
 Caux E., et al., 2011, *A&A*, **532**, A23
 Cazaux S., Tielens A. G. G. M., Ceccarelli C., Castets A., Wakelam V., Caux E., Parise B., Teyssier D., 2003, *ApJ*, **593**, L51
 Ceccarelli C., 2004, in Johnstone D., Adams F. C., Lin D. N. C., Neufeld D. A., Ostriker E. C., eds, *Astronomical Society of the Pacific Conference Series* Vol. 323, *Star Formation in the Interstellar Medium: In Honor of David Hollenbach*. p. 195
 Ceccarelli C., Loinard L., Castets A., Tielens A. G. G. M., Caux E., 2000, *A&A*, **357**, L9
 Ceccarelli C., et al., 2010, *A&A*, **521**, L22
 Ceccarelli C., Dominik C., López-Sepulcre A., Kama M., Padovani M., Caux E., Caselli P., 2014, *ApJ*, **790**, L1
 Ceccarelli C., et al., 2023, in Inutsuka S., Aikawa Y., Muto T., Tomida K., Tamura M., eds, *Astronomical Society of the Pacific Conference Series* Vol. 534, *Astronomical Society of the Pacific Conference Series*. p. 379
 Cernicharo J., Agúndez M., Kaiser R. I., Cabezas C., Tercero B., Marcelino N., Pardo J. R., de Vicente P., 2021, *A&A*, **652**, L9
 Cernicharo J., Tercero B., Marcelino N., Agúndez M., de Vicente P., 2023, *A&A*, **674**, L4
 Chandler C. J., Brogan C. L., Shirley Y. L., Loinard L., 2005, *ApJ*, **632**, 371
 Codella C., et al., 2017, *Astronomy & Astrophysics*, **605**, L3
 Codella C., et al., 2020, *Astronomy & Astrophysics*, **635**, A17
 Crapsi A., Caselli P., Walmsley C. M., Myers P. C., Tafalla M., Lee C. W., Bourke T. L., 2005, *ApJ*, **619**, 379
 Crapsi A., Caselli P., Walmsley M. C., Tafalla M., 2007, *A&A*, **470**, 221
 Crimier N., Ceccarelli C., Maret S., Bottinelli S., Caux E., Kahane C., Lis D. C., Olofsson J., 2010, *A&A*, **519**, A65
 Drozdovskaya M. N., et al., 2018, *MNRAS*, **476**, 4949
 Dzib S. A., Loinard L., Ortiz-León G. N., Rodríguez L. F., Galli P. A. B., 2018, *ApJ*, **867**, 151
 Endres C. P., Schlemmer S., Schilke P., Stutzki J., Müller H. S. P., 2016, *Journal of Molecular Spectroscopy*, **327**, 95
 Favre C., et al., 2018, *ApJ*, **862**, L2
 Fedoseev G., Li X., Baratta G. A., Palumbo M. E., Chuang K. J., 2025, *A&A*, **693**, A277
 Fuentetaja R., et al., 2023, *A&A*, **671**, L6
 Galli P. A. B., et al., 2019, *A&A*, **630**, A137
 Geppert W. D., et al., 2004, *ApJ*, **613**, 1302
 Giani L., Ceccarelli C., Mancini L., Bianchi E., Pirani F., Rosi M., Balucani N., 2023, *Monthly Notices of the Royal Astronomical Society*, **526**, 4535
 Giani L., et al., 2025, *MNRAS*, **537**, 3861
 Giers K., et al., 2022, *A&A*, **664**, A119
 Giers K., et al., 2023, *A&A*, **676**, A78
 Gottlieb C. A., Gottlieb E. W., Thaddeus P., Kawamura H., 1983, *ApJ*, **275**, 916
 Gottlieb C. A., McCarthy M. C., Thaddeus P., 2010, *ApJS*, **189**, 261
 Gupta H., Gottlieb C. A., McCarthy M. C., Thaddeus P., 2009, *ApJ*, **691**, 1494
 Güsten R., Nyman L. Å., Schilke P., Menten K., Cesarsky C., Booth R., 2006, *A&A*, **454**, L13
 Herbst E., van Dishoeck E. F., 2009, *ARA&A*, **47**, 427
 Hily-Blant P., Faure A., Vastel C., Magalhaes V., Lefloch B., Bachiller R., 2018, *MNRAS*, **480**, 1174
 Hiraoka K., Takayama T., Euchi A., Handa H., Sato T., 2000, *ApJ*, **532**, 1029
 Imai M., et al., 2016, *ApJ*, **830**, L37
 Jaber Al-Edhari A., et al., 2017, *A&A*, **597**, A40
 Jaber A. A., Ceccarelli C., Kahane C., Caux E., 2014, *ApJ*, **791**, 29
 Jacobsen S. K., Jørgensen J. K., Di Francesco J., Evans N. J., Choi M., Lee J.-E., 2019, *A&A*, **629**, A29
 Jenkins E. B., 2009, *ApJ*, **700**, 1299
 Jensen S. S., Spezzano S., Caselli P., Grassi T., Haugbølle T., 2023, *A&A*, **675**, A34
 Jiménez-Serra I., et al., 2016, *ApJ*, **830**, L6
 Jørgensen J. K., et al., 2016, *A&A*, **595**, A117

Jørgensen J. K., et al., 2018, [A&A](#), **620**, A170

Kahle K. A., Hernández-Gómez A., Wyrowski F., Menten K. M., 2023, [A&A](#), **673**, A143

Keto E., Caselli P., 2008, [ApJ](#), **683**, 238

Keto E., Caselli P., 2010, [MNRAS](#), **402**, 1625

Kirk J. M., et al., 2013, [MNRAS](#), **432**, 1424

Kobayashi H., Hidaka H., Lamberts T., Hama T., Kawakita H., Kästner J., Watanabe N., 2017, [ApJ](#), **837**, 155

Kuan Y.-J., et al., 2004, [ApJ](#), **616**, L27

Ladjelate B., et al., 2020, [A&A](#), **638**, A74

Lara-Moreno M., Stoecklin T., Halvick P., 2021, [MNRAS](#), **507**, 4086

Lin Y., Spezzano S., Sipilä O., Vasyunin A., Caselli P., 2022, [A&A](#), **665**, A131

Lindberg J. E., Charnley S. B., Cordiner M. A., 2016, [ApJ](#), **833**, L14

Loinard L., Castets A., Ceccarelli C., Tielens A. G. G. M., Faure A., Caux E., Duvert G., 2000, [A&A](#), **359**, 1169

Loinard L., Castets A., Ceccarelli C., Caux E., Tielens A. G. G. M., 2001, [ApJ](#), **552**, L163

Loison J.-C., Wakelam V., Hickson K. M., Bergeat A., Mereau R., 2014a, [MNRAS](#), **437**, 930

Loison J.-C., Wakelam V., Hickson K. M., 2014b, *Monthly Notices of the Royal Astronomical Society*, **443**, 398

Loison J.-C., et al., 2017, [MNRAS](#), **470**, 4075

Mangum J. G., Wootten A., 1990, [A&A](#), **239**, 319

Manigand S., et al., 2021, [A&A](#), **645**, A53

Maureira M. J., Pineda J. E., Segura-Cox D. M., Caselli P., Testi L., Lodato G., Loinard L., Hernández-Gómez A., 2020, [ApJ](#), **897**, 59

McCarthy M. C., Chen W., Apponi A. J., Gottlieb C. A., Thaddeus P., 1999, [ApJ](#), **520**, 158

McGuire B. A., et al., 2020, [ApJ](#), **900**, L10

McKeegan K. D., et al., 2011, [Science](#), **332**, 1528

Mikami H., Yamamoto S., Saito S., Guelin M., 1989, [A&A](#), **217**, L5

Millar T. J., Walsh C., Van de Sande M., Markwick A. J., 2024, [A&A](#), **682**, A109

Molpeceres G., Rivilla V. M., 2022, [A&A](#), **665**, A27

Müller H. S. P., Thorwirth S., Roth D. A., Winnewisser G., 2001, [A&A](#), **370**, L49

Müller H. S. P., Schlöder F., Stutzki J., Winnewisser G., 2005, *Journal of Molecular Structure*, **742**, 215

Müller H. S. P., Jørgensen J. K., Guillemin J.-C., Lewen F., Schlemmer S., 2023, [MNRAS](#), **518**, 185

Mundy L. G., Wootten A., Wilking B. A., Blake G. A., Sargent A. I., 1992, [ApJ](#), **385**, 306

Nagy Z., Spezzano S., Caselli P., Vasyunin A., Tafalla M., Bizzocchi L., Prudenzano D., Redaelli E., 2019, [A&A](#), **630**, A136

Neufeld D., et al., 2015, *Astronomy & Astrophysics*, **577**, A49

Okuda Y., et al., 2023, [ApJ](#), **948**, 127

Oya Y., et al., 2017, [ApJ](#), **837**, 174

Oyama T., Ozaki H., Sumiyoshi Y., Araki M., Takano S., Kuze N., Tsukiyama K., 2020, [ApJ](#), **890**, 39

Pickett H. M., Poynter R. L., Cohen E. A., Delitsky M. L., Pearson J. C., Müller H. S. P., 1998, *J. Quant. Spectrosc. Radiative Transfer*, **60**, 883

Podio L., Lefloch B., Ceccarelli C., Codella C., Bachiller R., 2014, [A&A](#), **565**, A64

Punanova A., et al., 2018, [ApJ](#), **855**, 112

Raaphorst M. T., Enrique-Romero J., Lamberts T., 2025, *arXiv e-prints*, p. [arXiv:2505.19908](#)

Redaelli E., Sipilä O., Padovani M., Caselli P., Galli D., Ivlev A. V., 2021, [A&A](#), **656**, A109

Redaelli E., et al., 2025, *arXiv e-prints*, p. [arXiv:2508.18848](#)

Remijan A., et al., 2023, [ApJ](#), **944**, L45

Sabatini G., Bovino S., Redaelli E., 2023, [ApJ](#), **947**, L18

Sahnoun E., Ben Khalifa M., Khadri F., Hammami K., 2020, [Ap&SS](#), **365**, 183

Sakai N., Yamamoto S., 2013, [Chemical Reviews](#), **113**, 8981

Sakai N., Sakai T., Hirota T., Yamamoto S., 2008, [ApJ](#), **672**, 371

Sakai N., Sakai T., Hirota T., Burton M., Yamamoto S., 2009, [ApJ](#), **697**, 769

Schöier F. L., van der Tak F. F. S., van Dishoeck E. F., Black J. H., 2005, [A&A](#), **432**, 369

Scibelli S., Shirley Y., Megías A., Jiménez-Serra I., 2024, [MNRAS](#), **533**, 4104

Siebert M. A., et al., 2022, [ApJ](#), **924**, 21

Silva W. G. D. P., et al., 2023, [A&A](#), **676**, L1

Sita M. L., et al., 2022, [ApJ](#), **938**, L12

Skouteris D., Balucani N., Ceccarelli C., Vazart F., Puzzarini C., Barone V., Codella C., Lefloch B., 2018, *The Astrophysical Journal*, **854**, 135

Socci A., Sabatini G., Padovani M., Bovino S., Hacar A., 2024, [A&A](#), **687**, A70

Spezzano S., Bizzocchi L., Caselli P., Harju J., Brünken S., 2016, [A&A](#), **592**, L11

Spezzano S., Caselli P., Bizzocchi L., Giuliano B. M., Lattanzi V., 2017, [A&A](#), **606**, A82

Stahler S. W., Palla F., 2004, *The Formation of Stars*

Suzuki H., Yamamoto S., Ohishi M., Kaifu N., Ishikawa S.-I., Hirahara Y., Takano S., 1992, [ApJ](#), **392**, 551

Tafalla M., Mardones D., Myers P. C., Caselli P., Bachiller R., Benson P. J., 1998, [ApJ](#), **504**, 900

Taniguchi K., Gorai P., Tan J. C., 2024, [Ap&SS](#), **369**, 34

Tinacci L., Ferrada-Chamorro S., Ceccarelli C., Pantaleone S., Ascenzi D., Maranzana A., Balucani N., Ugliengo P., 2023, [ApJS](#), **266**, 38

Urso R. G., et al., 2019, [A&A](#), **628**, A72

Vastel C., Ceccarelli C., Lefloch B., Bachiller R., 2014, [ApJ](#), **795**, L2

Vastel C., Ceccarelli C., Lefloch B., Bachiller R., 2016, [A&A](#), **591**, L2

Vastel C., Kawaguchi K., Quénard D., Ohishi M., Lefloch B., Bachiller R., Müller H. S. P., 2018a, [MNRAS](#), **474**, L76

Vastel C., et al., 2018b, [MNRAS](#), **478**, 5514

Vastel C., Loison J. C., Wakelam V., Lefloch B., 2019, [A&A](#), **625**, A91

Vazart F., Calderini D., Puzzarini C., Skouteris D., Barone V., 2016, *Journal of chemical theory and computation*, **12**, 5385

Vazart F., Ceccarelli C., Balucani N., Bianchi E., Skouteris D., 2020, *Monthly Notices of the Royal Astronomical Society*, **499**, 5547

Wakelam V., Selsis F., Herbst E., Caselli P., 2005, *Astronomy & Astrophysics*, **444**, 883

Wakelam V., Herbst E., Le Bourlot J., Hersant F., Selsis F., Guilloteau S., 2010, *Astronomy & Astrophysics*, **517**, A21

Wakelam V., Gratier P., Loison J. C., Hickson K. M., Penguen J., Mechineau A., 2024, *Astronomy & Astrophysics*, **689**, A63

Walker K. M., Lique F., Dawes R., 2018, [MNRAS](#), **473**, 1407

Ward-Thompson D., Motte F., Andre P., 1999, [MNRAS](#), **305**, 143

Wenzel G., et al., 2025a, [Nature Astronomy](#), **9**, 262

Wenzel G., et al., 2025b, [ApJ](#), **984**, L36

Xue C., et al., 2025, *arXiv e-prints*, p. [arXiv:2509.06256](#)

Yamamoto S., Saito S., 1994, [J. Chem. Phys.](#), **101**, 5484

Yamamoto S., Saito S., Kawaguchi K., Kaifu N., Suzuki H., Ohishi M., 1987, [ApJ](#), **317**, L119

Yamamoto S., Saito S., Kawaguchi K., Chikada Y., Suzuki H., Kaifu N., Ishikawa S.-I., Ohishi M., 1990, [ApJ](#), **361**, 318

van Dishoeck E. F., Blake G. A., Jansen D. J., Groesbeck T. D., 1995a, [ApJ](#), **447**, 760

van Dishoeck E. F., Blake G. A., Jansen D. J., Groesbeck T. D., 1995b, [ApJ](#), **447**, 760

van der Wiel M. H. D., et al., 2019, [A&A](#), **626**, A93

APPENDIX A: INCOMPLETE ION-NEUTRAL CHEMISTRY IN CYANOPOLYYNE NETWORKS

Astrochemical reaction networks are typically based on the two most widely used databases, (Kinetic Database for Astrochemistry: [Wake-
lam et al. 2024](#)) and UDfA (UMIST Database for Astrochemistry: [Millar et al. 2024](#)). The GRETOPABE network adopted in this work is also KIDA-based, updated with recent results from our group and others on selected iCOMs (e.g. [Loison et al. 2014b](#); [Neufeld et al. 2015](#); [Balucani et al. 2015](#); [Vazart et al. 2016](#); [Skouteris et al. 2018](#); [Vazart et al. 2020](#); [Codella et al. 2020](#); [Blázquez et al. 2020](#); [Giani et al. 2024](#)).

et al. 2023). Nevertheless, for many complex species with limited experimental and theoretical studies, such as cyanopolyyynes, the networks remain incomplete, leading to large uncertainties in model predictions. For example, as one moves from HC_3N to HC_{11}N , the number of known production reactions decreases drastically (from 46 to 27). While the neutral–neutral chemistry of HC_5N has recently been revised (Giani et al. 2025), the ion–neutral pathways remain poorly constrained. Ionic reactions thought to be relevant for HC_nN formation, particularly at times $<10^5$ years, include the electron recombination processes $\text{HC}_n\text{NH}^+ + \text{e}^-$ and $\text{H}_3\text{C}_n\text{N}^+ + \text{e}^-$ (Geppert et al. 2004; Loison et al. 2017), yet the networks of the corresponding protonated precursors are largely incomplete. For instance, current databases list 28 formation reactions for HC_3NH^+ , five for HC_5NH^+ , and only four for HC_7NH^+ and HC_9NH^+ . In the case of $\text{H}_3\text{C}_n\text{N}^+$ ions, four reactions are listed for each species, but none have been studied theoretically or experimentally, and identical rates and products are assumed in each case. In our network, the formation reactions of HC_7NH^+ and HC_9NH^+ from HC_7N^+ and HC_9N^+ are missing, even though these are among the key reactions responsible for the formation of HC_3N and HC_5N . While the most recent updates of the KIDA and UDFa databases now include these reactions, their rate coefficients remain uninvestigated. We therefore suggest revising both the formation reactions of HC_nNH^+ , namely, $\text{HC}_n\text{N}^+ + \text{H}_2$, and those leading to HC_nN^+ itself, such as $\text{C}_n\text{H}_3^+ + \text{N}$ and $\text{C}_n\text{N}^+ + \text{H}_2$. The omission of these reactions, as well as the use of uncertain rate coefficients, may explain why our models underestimate the abundances of the larger cyanopolyyynes. In particular, we expect that including these missing pathways could reduce the discrepancy of about one to two orders of magnitude between the model predictions and the observed abundances of the longer cyanopolyyynes. However, arbitrarily adding reactions without properly revising their products and rates would introduce even larger uncertainties. We therefore strongly recommend a systematic revision of the ionic chemistry of cyanopolyyynes to make their formation networks more complete, a task we plan to address in future work.

This paper has been typeset from a $\text{\TeX}/\text{\LaTeX}$ file prepared by the author.